Université d'Ottawa | University of Ottawa

Department of Biomedical Mechanical Engineering

Faculty of Graduate and Postdoctoral Studies

Cellular Response to Semi-ordered and Biomimetic Nanotubular Surfaces

Supervisor: Dr. Fabio Variola

Thesis submitted in partial fulfillment of the requirements for the Master of Applied Science degree in Biomedical Engineering

TABLE OF CONTENTS

Table of Contents ii
List of Abbreviations iii
List of Figures iv
List of Tables vi
Acknowledgements vii
Abstract viii
Chapter 1: Introduction 1
1.1 Motivation 1
1.2 Main Objectives 2
1.3 Specific Objectives 3
1.4 Relevance 4
1.5 Background 5
1.5.1 Nanotubular titanium surfaces 5
1.5.2 Biomimetic Surfaces and Diatom Frustules 9
1.5.3 Spatial Statistics 11
1.5.4 Human mesenchymal stem cells (hMSCs) 12
1.5.5 Characterization of Cell Behavior 12
Chapter 2: Materials and Methods 23
2.1 Substrates preparation and characterization 23
2.2 Cell Cultures 26
Chapter 3: Results 28
3.1.1 Nanotubular Spatial Statistics 28
3.1.2 Wall Thickness 29
3.1.3 Atomic Force Microscopy 31
3.1.4 Contact Angle Analysis 31
3.1.5 Nearest Neighbor and Voronoi Analysis 33
3.1.6 Voronoi Defects 35
3.1.7 Stem Cell Proliferation 37

3.2.1 Cell Spreading and Morphology....38
3.2.2 Focal Adhesion Analysis....40
3.2.3 Nuclear Elongation....42
3.2.4 Osteogenic Potential....44
3.2.5 Scanning Electron Microscopy of Filopodia....46
Chapter 4: Discussion....47
4.1 Nanotubular Morphology and Spatial Statistics....47
4.2 Cellular Studies....52
Conclusions and Future Outlook....56

List of Abbreviations

BI Biomimetic

SEM Scanning Electron Microscopy

AFM Atomic Force Microscopy

NND Nearest Neighbor Distance

MSC Mesenchymal Stem Cell

VCA Voronoi Cell Area

ECM Extracellular Matrix

FA Focal Adhesion

FAK Focal Adhesion Kinase

VASP Vasodilator-stimulated Phosphoprotein

LINC Linker of Nucleoskeleton and Cytoskeleton

OSX Osterix

OPN Osteopontin

OCN Osteocalcin

List of Figures

Figure 1 Scheme representing an electrochemical cell used to produce TiO2 films.....7

Figure 2 The oxide formation/dissolution equilibria 8

Figure 3 The electrochemical anodization process and possible anodic morphologies 9

Figure 4 Sample of diatom species morphology.....10

Figure 5 Schematic diagram which shows adhesion maturation 15

Figure 6 The nanoscale structure of a focal adhesion.....16

Figure 7 The stages of cell spreading and adhesion 16

Figure 8 Model of cell spreading and polarization 17

Figure 9 Cell shape and spreading area affect nuclear morphology.....18

Figure 10 Mesenchymal stem cell differentiation and self-renewal.....20

Figure 11 Surface of layers of self-aligned TiO2 nanotubes with different diameters.....22

Figure 12 Osteopontin (OPN) and Osteocalcin (OCN) staining of osteoprogenitor cells after twenty-one days of culture.....23

Figure 13 Schematic for a two-step anodization of titanium nanotubes.....24

Figure 14 SEM top-views of the nanotubular layers of different tube diameters.....29

Figure 15 Nanotube diameter distributions for separate conditions 30

Figure 16 Atomic force microscopy images of the different sets of nanotubes 31

Figure 17 Contact angle analysis of the different nanotube conditions.....32

Figure 18 Normalized nearest neighbor distance and Voronoi cell area compared to expected perfectly ordered and random (disordered) computer generated models 34

Figure 19 Local innertube order between BI 20 and 20 nm surfaces 35

Figure 20 Voronoi defect example images 36

Figure 21 Cell proliferation counts for differential timepoints.....37
Figure 22 Box plots of cell area for differential timepoints.....39
Figure 23 Box plots of form factor calculations of stem cells on nanotubular titanium for differential timepoints.....39
Figure 24 Cell morphology of cells in culture for 48 h 40
Figure 25 Focal adhesion analytics for differential nanotube morphologies.....41
Figure 26 Nuclei major axis length for nanotubular conditions after 48 h.....43
Figure 27 Osteogenic differentiation through OSX staining 44
Figure 28 Alizarin red staining of nanotubular conditions 45
Figure 29 Optical microscope images of alizarin red stained nanotubular conditions. 45
Figure 30 SEM micrographs of filopodia on nanotube conditions.....46
Figure 31 Peak position and width parameter of photoactivatable fluorescent proteins fusions in focal adhesions.....50

List of Tables

Table 1 Formation conditions for different nanotubular surfaces on titanium 24

Table 2 Wall thickness of nanotubes measured from SEM images.....30

Table 3 Contact angle values for differential nanotubular conditions.....32

Table 4 Nearest neighbor distance as a function of nanotubular layer diameter.....35

Table 5 Voronoi defects as a function of nanotubular layer diameter.....36

Table 6 Cell proliferation and growth change 38

Table 7 Average focal adhesion lengths 42

Table 8 Average focal adhesion lengths (large) 42

Table 9 Summary of the geometric analysis.....59

Table 10 Summary of the cellular analysis.....59

Acknowledgements

I would like to thank my supervisor, Dr. Fabio Variola, for his great guidance, vision and tutelage during my time at the University of Ottawa. Additionally, I would like to thank my lab colleague Alex Steeves for sharing his experience and for teaching stem cell culture techniques, as well as Yun Liu and Glenn Poirier for their wonderful help with SEM characterization. Finally, I would like to thank Dr. Chloë van Oostende-Triplet and Skye McBride for their patience and support with instruction on cellular imaging techniques. This work was supported by NSERC through the Discovery grant, by the Canada Foundation for Innovation (CFI) and the Ontario Ministry of Research and Innovation (MRI) through the Leaders of Opportunity (LOF) fund.

Abstract

Understanding cell behavior at the material-host tissue interface is a fundamental prerequisite for designing the next generation of biomaterials capable of directing cellular events towards a desired biological outcome (e.g. faster tissue integration). In addition, unraveling the relationship between cell activity and nanoscale surface features will further the present knowledge of the fundamental cellular mechanisms that control how cells sense and respond to natural (e.g. extracellular matrix) and synthetic (e.g. biomaterials) surfaces. It is now well-known that the nanoscale physicochemical features of surfaces dictate cell fate by affecting phenomena such as proliferation, differentiation, genetic transcription and protein translation. In particular, nanotopographical features play a pivotal role during cell-surface interactions by exerting a direct mechanotransductive effect on cells, which, in turn, dictate biochemical signaling. In this context, several studies have addressed different aspects of the relationships between nanofeatures and specific cellular functions, including morphological changes, the establishment of focal adhesions (FAs, clusters of adhesion molecules that regulate cell structure and activity, determining how cells sense and respond to natural and synthetic substrates) and differentiation. However, the precise interplay between the morphological characteristics of nontopographical features not only on the surface but also along a third dimension (height) and cellular response still needs to be fully elucidated. Once revealed, such knowledge will shed new light on how cells sense and respond to 2- and 3-dimensional nanoscale patterns. In this context, anodization, a simple yet effective electrochemical treatment, allows to engender on titanium, the gold standard in medicine, arrays of nanotubes with tailor-made diameters. Notably, although nanotubular surfaces on anodized titanium have been extensively studied in relation to their effect on cell response, none of the previous studies has precisely assessed the effects of the morphological features and geometrical

arrangement of the nanotubes. This is an important aspect, since the morphological characteristics and the spatial placement of nanofeatures has been shown to control cell response. In addition, by employing the same technique (i.e. anodization), a 3-dimensional hierarchical surface that mimics the frustule (i.e. silicified cell wall) of diatoms (a type of microalgae) can be created. Aside from enabling, for the first time, cellular studies on such bioinspired surface, this hierarchical nanoscale substrate will also allow to probe the effects of a 2-tier nanotopographical gradient along the depth of the nanotubular layer.

CHAPTER 1: INTRODUCTION

In recent years there has been ample interest in nanoscale modifications of materials to understand fundamental cell functions and ultimately control cell response for improve biological outcomes. Nanostructured surfaces provide the ideal substrate to investigate the mechanisms that control cellular functions on synthetic materials. Through the understanding of cell-surface interactions and their effects on cell viability and functions, wide-ranging uses in implant design and control of stem cell differentiation for injury and disease may spring forth.

1.1 Motivation

This study aims at closing in on the mechanisms that control how cells respond to nanotopographical surfaces, a fundamental aspect in expanding the present knowledge of cell-surface interactions. In addition, this research will address, for the first time, the cellular response to a biomimetic surface created on titanium by a simple yet effective electrochemical treatment. It is known that nanotopographical features exert direct mechanotransductive effects and trigger biochemical signaling events in cells. However, most previous studies have focused on size effects

(i.e. nanotube diameter) on cellular proliferation and differentiation, without special note given to spatial arrangement, nor biomimetic nanosurfaces. The detailed study of spatial order of nanoscale features as well as interactions with a third nanoscale dimension will help bridge these gaps and provide further information on stem cell response. Furthermore, the three-dimensional surface created for this study mimics biologically successful hierarchical surface structures of diatoms, and a nanoscale study is of great interest in discussing the fractal, repetitive nature of these successful biological structures. Finally, as stem cells are multipotent cells with the ability to differentiate into nearly any other cell, the potential for differentiation is of tremendous importance to delineate, especially if this capability is under a set of controls at the nanoscale.

Therefore, the study will aim at precisely elucidating the effects of (*i*) morphology, (*ii*) spatial arrangement and (*iii*) extradimensional parameters on human mesenchymal stem cells sense as well as the (*iv*) bioactive relevance of a novel biomimetic nanostructure through cellular studies. Of note, the bio-inspired component to this study opens up new avenues in both understanding hierarchical structures in nature as well as how a simple anodization process can create these complex periodic structures for applications of both fundamental and practical importance. Of note, to date, this surface has only been made by more complex techniques (e.g. two photon lithography, atomic layer deposition).

1.2 Main Objectives

The main objectives of this study are to (*i*) apply anodization to a medically relevant metal in order to tune the nanotopography of nanotubular surfaces and generate a biomimetic substrate, (*ii*)

apply spatial statistics to quantitatively characterize the surfaces' order/disorder[1], (*iii*) characterize other relevant physicochemical parameters and (*iv*) carry out stem cell studies at short- and longer-term intervals.

1.3 Specific Objectives

In particular, four different nanotube conditions will be created: a 'small' (~ 20 nm diameter), 'intermediate' (~ 60 nm diameter), 'large' (~ 100 nm diameter) and 'biomimetic' (obtained by overlaying the small and large conditions upon each other, mimicking the naturally occurring structure of diatom frustules).

(1) Geometrical and physical descriptors for these nanostructured substrates (e.g. degree of order, nanotube diameter and spacing, wettability) will be quantified by (*i*) applying spatial statistics approaches (i.e. nearest neighbor distance, Voronoi analysis) to scanning electron microscopy (SEM) images, (*ii*) using atomic force microscopy (AFM) and (*iii*) carrying out contact angle measurements.

(2) Successively, the cellular effects including stem cell proliferation, morphology and differentiation on the tailor-made nanotubular surfaces over three time points will be assessed. In particular, epifluorescence, confocal microscopy and SEM will be used to close in on the cellular response to determine how this varies in relation to changes of the nanotube characteristics.

[1] Disorder has previously been shown to induce osteogenesis in stem cells[12], but the disorder parameter itself has not been characterized thoroughly in the literature.

1.4 Relevance

It is of crucial importance for scientists to control nanofeatures on medically relevant materials such as titanium. For example, there is great interest in creating and controlling nanoscale surface features and understanding the cell response for shedding new light on the mechanisms that control how cells sense and respond to synthetic surfaces. In the longer term, this is a critical prerequisite that will allow to improve biomedical implants towards a faster and more stable integration in tissues. Achieving the ability to fine tune surface nanotopography and elicit specific biological functions promise to ultimately provide a 'translational shortcut' both intuitive and parsimonious. Furthermore, the study of biomimetic surfaces which mimic successful biological organisms may unlock aspects that can be successively applied to various technological fields in addition to biomedical applications.

In this context, titanium is the gold standard metal in medicine. It is widely used for dental and orthopedic implants to overcome detrimental conditions associated with disease, aging and trauma.[1] The critical factors determining the application of the material for biomedical implants are its bio-compatibility and corrosion resistance, two characteristics that are associated with the native oxide layer that forms on titanium-based metals. However, despite its natural biocompatibility, when titanium is implanted in the body, fibrous encapsulation (i.e. formation of a soft tissue sheath at the bone-implant interface) may occur, ultimately hindering stable bone integration. For this reason, there has been great interest towards methods that improve bio-compatibility/integration through nanoscale surface modifications.[1,2] In this context, simple anodization procedures can produce ordered nanotubular structures of varying size, capable of positively influence cell behaviour[3].

In this context, we have capitalized on the distinctive potential of anodization to engender tunable nanometric features towards nanoscale platforms to distinctively unveil the precise correlation between the morphology and geometrical arrangement of nanotubes and mesenchymal stem cell response. To this end, we learnt to create differentially sized nanopatterns with a facile anodization technique, which through the rational manipulation of parameters also allowed the creation of a novel biomimetic hierarchical surface. Nature provides in fact fantastic inspiration for new materials.[4,5] Among these, the frustule of diatoms has gathered much interest for new materials, photovoltaics and microfluidics because of their hierarchical surface micro- and nano-structure.[6–8] Since cells are known to benefit from nanostructures, we reproduced a similar structure to the diatom surface at the nanoscale. We successively decided to evaluate the cellular response to these surfaces, a research question that has never been addressed before. Through correlation of spatial statistics to the stem cell response (including proliferation, morphology and differentiation), as well as investigating the response to a biomimetic surface, important new information regarding stem cell-nanostructure interactions were delineated.

Ultimately, results from this work strengthen the role of direct physicochemical cueing to unlock the potential to affect healing and controlling stem cell fate, paving the way to combine both physical and chemical cues in a synergistic manner for drastically improved, efficient and effective biological outcomes of implantable materials.

1.5 Background

1.5.1 Nanotubular titanium surfaces

Titanium is widely used in dental implants and orthopedics (joint replacements and bone pins, plates and screws). Of note, 40% of today's biomedical implant materials based on titanium or its

alloys.[2,9] There is great interest in nanotopographical modification of titanium for research and use in biomedical implants and drug delivery systems, since nanometric surface features have demonstrated to endow materials with new exciting properties.[2] Of note, currently there are numerous commercial dental implants which display surface nanofeatures (e.g. nanoroughness and nanoparticulates) marketed toward improved ossointegration.[10] However, these do not provide the morphological accuracy necessary to precisely correlate specific topographical parameter to cell response. In this context, arrays of nanotubes created by a simple yet effective electrochemical treatment (i.e. anodization) are another one of the most prominent examples of how nanoscale features can be precisely designed on commercially available metals, enabling a variety of studies which highlighted fundamental cell behavior[11,12](see section 1.5.6). In particular, the resulting nanotubular layer has shown to enhance a variety of cellular functions *in vitro*[13], while also simultaneously providing a promising strategy for ossointegration *in vivo*.[13]

Anodization is an electrochemical process which alters the native protective oxide layer of passive metals (e.g. titanium, aluminum) as a consequence of impressed current circulating in an electrochemical cell. In this case, a metallic electrode (in our case titanium) is connected to the positive pole of a DC power supply and a platinum counterelectrode is connected to the negative pole (Figure 1). When a potential is applied in electrolytic solution the metal reacts with oxygen ions from the electrolyte, producing a thicker oxide layer with hollow features composed by TiO_2 nanotubes.

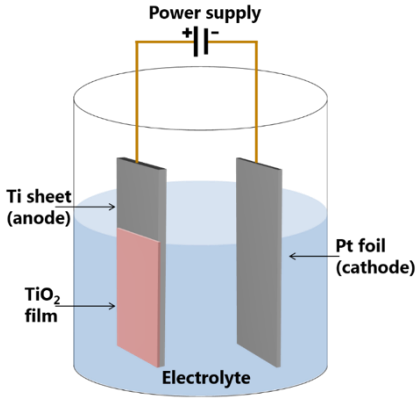

Figure 1. Scheme representing an electrochemical cell used to produce TiO_2 films by anodization of Ti. From reference[14].

Titanium oxide nanotubes can be grown in electrolytes containing fluoride, as described by the balance of two competitive reactions establishing an oxide formation/dissolution equilibrium (Figure 2):

$$Ti + 2H_2O \rightarrow TiO_2 + 4H^+ + 4e$$

(anodic oxidation)

and

$$TiO_2 + 4H^+ + 6F^- \rightarrow TiF_6^{2-} + 2H_2O$$

(chemical dissolution)[15]

The oxide must be soluble in the electrolyte to provide continuous oxide growth for the nanotubes to form: in the case of titanium-based metals, this is achieved by the addition of fluoride ions (either as HF or NH_4F) which solvatizes the native TiO_2 as fluoride complexes via chemical dissolution or by capturing Ti ejected to the electrolyte by complexation as TiF_6^{2-}. If the dissolution rate is too high, no steady-state oxide layer is formed and the oxide will be completely dissolved.

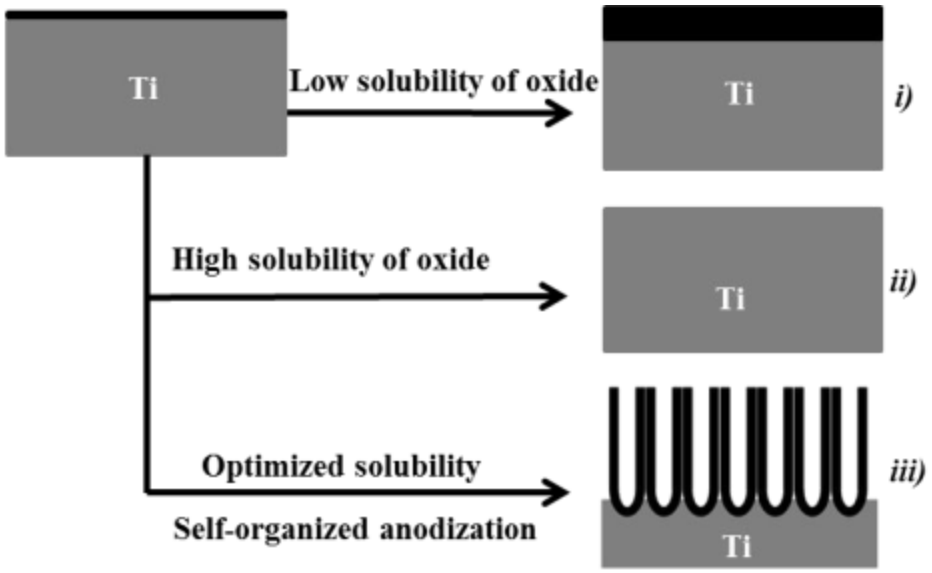

Figure 2. The oxide formation/dissolution equilibria. *i*) If the oxide is not soluble in electrolyte, as the anodization progresses and the oxide layer formed grows thicker, the field will decrease, eventually diminishing to the point where ion migration stops. *ii*) If the oxide is highly soluble complete dissolution occurs (electropolishing). *iii*) If the oxide dissolution and formation reach a steady-state, self-organized structures such as nanotubes may form. Figure from reference [16]

As to the reason behind why nanotubes result from this reaction, a leading theory suggests that the initial formation of a distinct tubular morphology is due to the buildup of compressive stress during the early phase of anodic oxide formation forming curved dimples in the oxide,[16] which create distinct loci with increased field concentration leading to higher dissolution (and tube nucleation) at those regions.

To optimize the order and spacing of the nanotubes, it has been shown that reducing the water content by utilizing ethylene glycol as the electrolyte can produce hexagonally arranged tube layers (Figure 3).[9,17] Additionally, initiation of the tubes' growth at preferential sites increases self-organization through a double anodization process: first, nanotubes are conventionally formed on the surface through anodization and then the TiO_2 nanotubular oxide layer is removed by adhesive

tape. The resulting oxide-stripped Ti surface contains well organized dimples (locations where the tube-ends were attached to Ti substrate) which constitute the preferential centers for growth of the tubes in the secondary anodization process.[18] It is this double anodization method which was used to produce the nanotubes for this study.

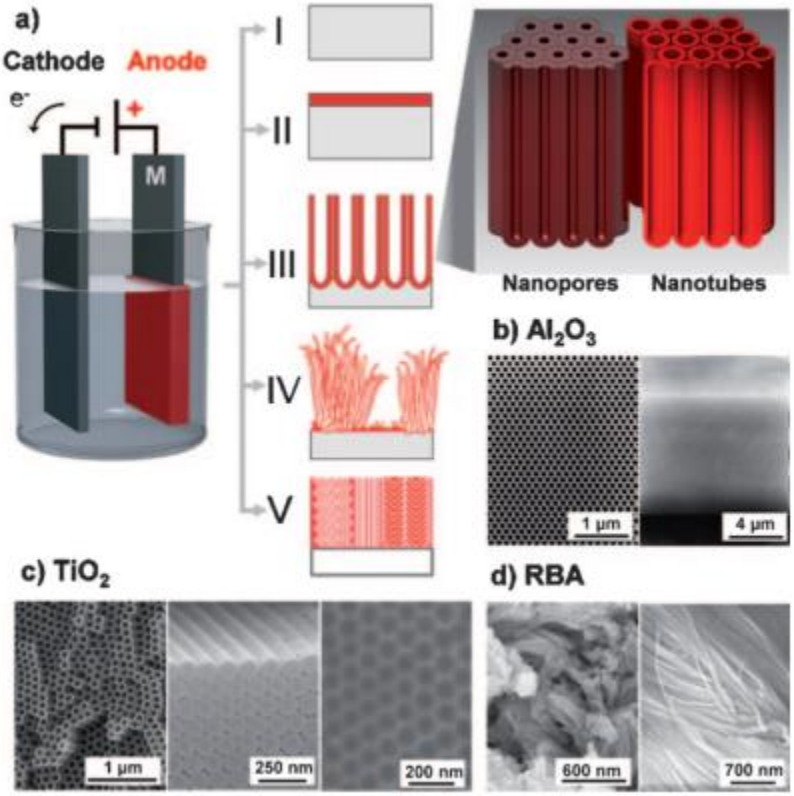

Figure 3. The electrochemical anodization process and possible anodic morphologies: a) I) metal electropolishing, II) formation of compact anodic oxides, III) self-ordered oxides (nanotubes or nanopores), IV) rapid (disorganized) oxide nanotube formation, V) ordered nanoporous layers. Examples of morphologies of obtained structures: b) Classical highly organized nanoporous alumina, c) highly ordered TiO_2 nanotubes (in top and side view) with dimpled structure (right) on metal surface when tubes are removed, d) disordered TiO_2 nanotubes growing in bundles. RBA= rapid-breakdown anodization. Figure from reference [9]

1.5.2 Biomimetic Surfaces and Diatom Frustules

Biomimetic surfaces can offer insights into material structure design, as nature can provide great inspiration from successful organisms. Diatoms are single-celled microscopic *algae* which

utilize porous hierarchical structures in their walls (frustules) (Figure 4). They are a very successful organism, with hundreds of thousands of species, each with unique shapes, and pore sizes which range from the nanometer to the micrometer scale.[19] There has been much interest in studying diatom biostructures to understand the unique properties of their nanostructured exoskeleton for nanotechnological applications such as drug delivery carriers, mechanical properties, optical and self-assembled devices; their 3-dimensional hierarchical structure plays a large role in this interest.[19,20,21] While previous studies focused on these applications of the hierarchical diatomic nanostructure, a biological study probing the effect on stem cells is lacking. Additionally, studies which sought to emulate the diatomic hierarchical nanostructure utilized complex, equipment-restricted techniques such as atomic layer deposition and two-photon lithography[21], which most of the times recreated these structures at the micrometric level. Conversely, a facile 2-step anodization has been found in our case to produce hierarchical nanostructures strikingly similar to the diatom. Our study will aim at probing the effect of such hierarchical nanostructures on the stem cells using a facile method of construction, and therefore add to the cell-nanostructure literature in a unique and novel way.

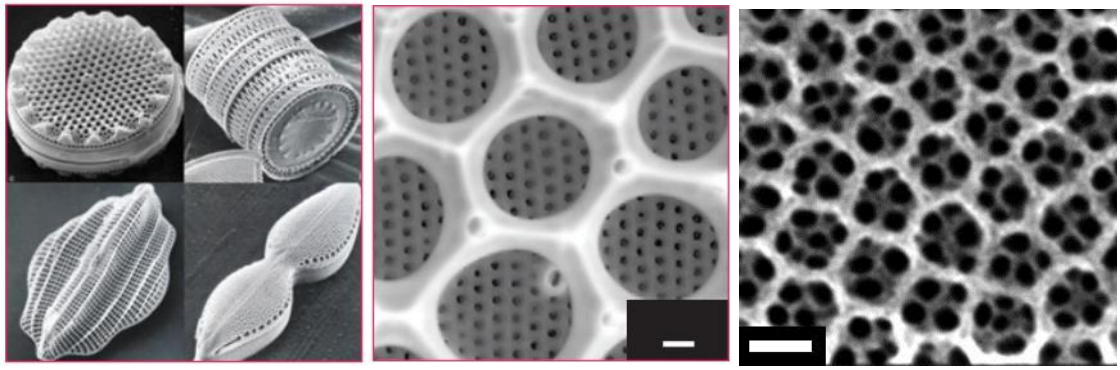

Figure 4. Sample of diatom species morphology (left), followed by a comparison of natural periodic lattice structure of diatom (middle), from reference [21], and our novel hierarchical TiO_2 nanotubular structure (right) characterized by the superimposition of a larger grid over a smaller lattice, and the addition of a height dimension. Scale bar: 20 microns (middle), 100 nm (right)

1.5.3 Spatial Statistics

The geometrical arrangement of arrays of nanotubes is not completely ordered, nor completely disordered. Quantifying order through geometric analysis such as Voronoi cell area and nearest neighbor distance (NND), in comparison with perfectly ordered, and randomly distributed surfaces may give additional insight into both the surface characteristics and their interaction with cellular biomechanics. In fact, it was shown[12] that the nanoscale disorder of nanoporous substrates can stimulate human mesenchymal stem cells (MSCs) to produce bone mineral *in vitro* in the absence of osteogenic supplements. Therefore, determining the degree of order/disorder of nanotubular TiO_2 surfaces is a fundamental prerequisite to fully understand their effects on stem cells.

Nearest Neighbor Distance

Nearest neighbor distance (NND) is a measure of the distance between each centroid and its nearest neighbor's centroid location. Each centroid has one nearest neighbor distance associated with it, and aggregation of many NND can provide a measure of degree of spacing or clustering. It is defined when given a set S of points in a space M and a query point $q \in M$, the closest point in S to q is identified.[22,23]

Voronoi Tessellation, Cell Area and Defects

Voronoi diagrams are a certain decomposition of a given space into cells, via a distance function and by a tuple of subset points $(Pk)k \in K$, called the generators or the sites.[24] Voronoi cell areas (VCA) are the areas of the partitioned Voronoi diagram of a surface in which every point in the VCA is nearer to no other generator site (in our case, the generators are the centroids of the nanotubes). [25] In other words, given a finite set of points {p1, …, pn}, a given point pk will have a corresponding Voronoi cell Rk which consists of every point in the Euclidean plane whose distance to pk is less than or equal to its distance to any other pk. Voronoi cells also have edges,

or sides, with each side corresponding to a nearest neighbor. In our case with optimal hexagonal spacing each Voronoi cell would have 6 edges (representing six nearest neighbors). Voronoi "defects" in our definition refers to the cells which have greater or less than 6 edges, and therefore occupying a suboptimal-ordered classification.

1.5.4 Human mesenchymal stem cells (hMSCs)

Stem cells are distinguished by an exceptional capability to differentiate into numerous types of cells. In particular, human mesenchymal stem cells (MSCs) are multipotent stromal cells capable of adipogenesis, chondrogenesis and osteogenesis.[26] These characteristics open new doors for many opportunities in tissue engineering and regenerative medicine. In vivo, stem cells reside within tissue-specific niches in the body; complex and controlled biochemical environments (including soluble chemokines, cytokines and growth factors, as well as insoluble transmembrane receptor ligands and extracellular matrix (ECM) molecules) which maintain their stem-cell fate (Figure 10).[27] Biophysical elements of the stem cell niche (including matrix mechanical properties, protein fibers and other topographical elements) also exert strong effects on stem cell maintenance and proliferation. Stem cells exit the niche when there is injury, in which thereby they proliferate, self-renew, and differentiate to heal the injured area.[28] For further exposition on the mechanisms which guide stem cells, we may utilize methods that isolate particular aspects of the complex stem cell niche (in this case, nano-spacing, geometry and height on the order of stem cell niche proteins).

1.5.5 Characterization of Cell Behavior

Focal Adhesions

Cell adhesion to the ECM is a sophisticated process which involves ECM-specific recognition by integrin transmembrane receptors, followed by aggregation with specific cytoplasmic proteins

into dense supramolecular complexes called focal adhesions (FAs).[29] Regulating adhesion and de-adhesion between cells and their surrounding ECM is critical for cell migration, and studies on adhesion can help shed light on embryonic development, immune responses, as well as tumour invasion, survival and cell proliferation.[30] FA-mediated adhesion was also shown for synthetic surfaces.[11] FAs are the multimeric protein complexes which connect the actin cytoskeleton to the ECM, and believed to be the regions where integrin-mediated mechanosensation takes place. The focal adhesion is closely tied to the actin cytoskeleton, which controls cellular structure and shape, protein transport as well as organization of organelles. Cells constantly probe the ECM surface through contractile and adhesive molecular machinery, namely integrins, which are a class of heterodimeric transmembrane receptor proteins embedded in the outer part of the cell membrane. Since integrins lack an actin binding site, other proteins are necessary for the FA-cytoskeleton linkage. Proteomic studies have identified over 500 FA associated proteins.[31] In addition to the chemical portion of the ECM, physical forces exert an influence on the interactions of FA proteins. Mechanical tension on each FA affects key steps including the elongation, reinforcement, and maintenance of FA structures. Furthermore, FA mechanotransduction is a major feature of cellular microenvironment sensing, including FA composition, morphology or signaling, leading to downstream changes in FA-dependent cellular functions, including gene expression. [29,32-33]

Integrins

Integrins are heterodimeric transmembrane proteins which perform chemical, physical, and topographical sensing as well as signaling functions for the cell.[34] As integrins do not possess enzymatic activity, their effect depends on their ability to recruit adhesome signaling components to activate signaling networks. Through specific combinations of a and b heterodimers, the molecular composition of the ECM (i.e. fibronectin, vitronectin, collagen, and laminin) and

physical properties (rigidity, ligand density, isotropy, and topography) can be sensed. This is a dynamic two-way process, as the expression of heterodimers can be changed over time in a fashion which alters cellular response to those proteins.[35,36]

Vinculin

The focal adhesion complex (Figure 6) contains hundreds of different proteins, notable of which is vinculin. Vinculin is a critical FA protein facilitating the molecular clutch linkage between ECM-bound integrins and actin; it has previously been shown that knocking down vinculin results in lower cellular traction forces.[37] The adaptor protein vinculin is key to the regulation of FAs.[38] It is structured by three major domains (an N-terminal head, flexible proline-rich hinge (neck) region, and a C-terminal tail domain) and its activation results from conformational changes in these domains. For example, when vinculin is recruited into a FA it changes to an open, active conformation. Research has shown that the interaction of the activated conformation of vinculin with another FA protein (i.e. talin) exerts a strong effect on integrins, clustering them in an active conformation which grows the FA to a larger size.[38] It is hypothesized that loading the talin-mediated linkage between integrin and actin recruits more vinculin, which also binds to actin to reinforce the molecular clutch.[37] As such, vinculin was chosen as the marker for fluorescent studies of focal adhesions in this work.

Adhesion Formation and growth

The current literature on integrin adhesions show four main phases of their evolution: nascent adhesions, focal complexes, focal adhesions, and fibrillar adhesions (Figure 5).[34] Nascent adhesions are miniscule structures (<0.5 microns) in size formed when initial interaction of integrins with talin takes place to enhance integrin-ECM binding and starts the process of integrin clustering.[39,40] The recruitment of additional adhesome proteins to the adhesion sites by myosin

grows the clusters into larger focal complexes (<1 micron diameter).[41] These focal complexes further progress with more protein recruitment into larger, elongated focal adhesions (1-5 micron diameter) and are located on the forward protrusion of migrating cells. The transformation of the nascent adhesion is concluded in the fibrillar adhesions (>5 microns), which have the ability to remodel the ECM and induce fibrillogenesis. Regulation of the evolution of focal adhesions is due to cell signaling by small GTPases, including Rac1, cdc42 (formation of focal complexes), and RhoA (focal adhesion maturation).[42]

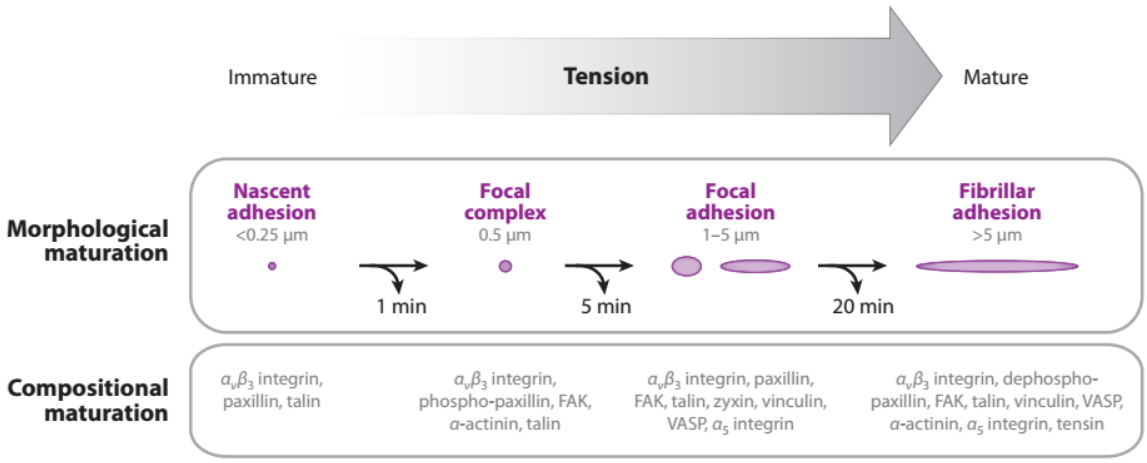

Figure 5. Schematic diagram which shows adhesion maturation (above), including morphological phases. Below: compositional stages of adhesion maturation in response to increasing mechanical tension (represented by the *gray arrow*). Additionally, adhesion turnover may occur (*curved black arrows with timescale for turnover*). FAK = focal adhesion kinase; VASP = vasodilator-stimulated phosphoprotein. Figure from reference[43]

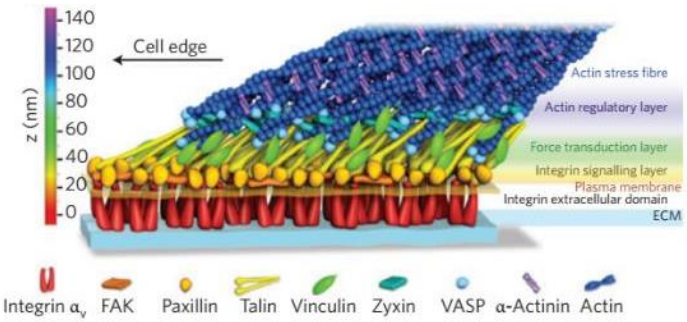

Figure 6. The nanoscale structure of a focal adhesion. Important components such as the integrin/extracellular binding domain, integrin signalling layer, force transduction layer and actin regulatory layer are displayed. FAK = focal adhesion kinase; VASP = vasodilator-stimulated phosphoprotein. Figure from reference[30]

Cell Spreading

Passive adhesion and spreading occurs within minutes after a cell encounters a surface (Figure 7). The shape change associated with cellular spreading necessitates the plasma membrane redistribution to conform with the new shape (Figure 8). This redistribution comes chiefly from the membrane reservoir, present at the surface of the cell.[44] Whether or not an adherent cell can spread has important consequences such as proliferation, quiescence or apoptosis.[45]

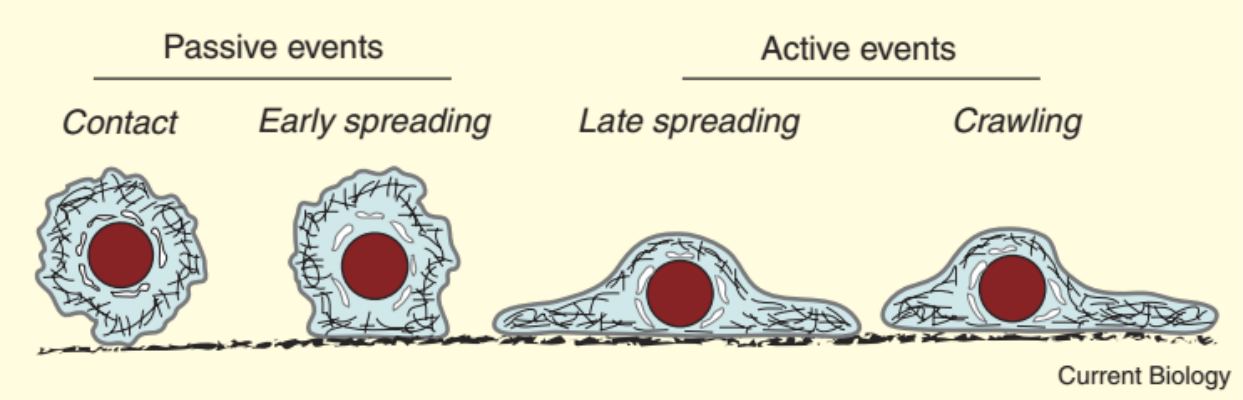

Figure 7. The stages of cell spreading and adhesion. Cell spreading and attachment early on do not require energy, however in later stages the active processes of actin polymerization and myosin contraction utilize metabolic energy and are essential for polarized cells to crawl. Figure from reference[45]

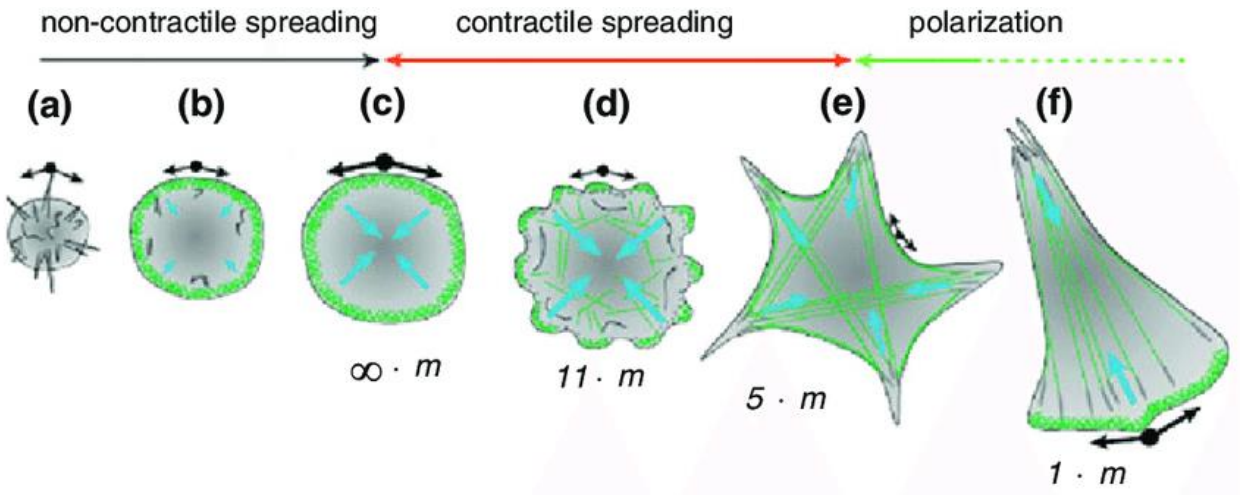

Figure 8. Model of cell spreading and polarization. (a) Rounded up cell with weak cell–substrate attachment. (b) Rapid and non-contractile phase of spreading, unfolding of the membrane reservoirs affords extra membrane area. (c) Spreading phase transition with entry into the contractile spreading phase. The membrane reservoirs are totally unfolded and give rise to an increase in membrane tension. Activation of exocytosis and myosin II-mediated contraction. (d) The leading edge of the cell becomes more heterogeneous with alternating protrusive and retractile regions. Stable adhesions start to mature at this stage. (e) The cell is now fully spread, actin bundles have matured into strong and clearly identifiable stress fibers linking focal adhesions. (f) The polarized phase. Lamellipodia protrude on one side of the cell, while the other side of the cell shrinks. Figure from reference[44]

Nuclei Elongation

It has been observed that nuclear shape is dependent on the aspect ratio of the cell, through experiments with 3T3 and A549 cells in confined geometries (Figure 9).[46] Nuclei have been found to exhibit favored alignment along the length of high aspect ratio rectangular patterns, which is explained by the fact that focal adhesions at the cell membrane transmits mechanical forces to nuclear LINC (Linker of Nucleoskeleton and Cytoskeleton, a protein complex involved in chromosomal movement and responding to extracellular stimuli[47]) complexes and lamina through the cytoskeleton. Studies have also shown that cells which are proliferating and cells which are quiescent differ in their nuclear architecture and chromosomal arrangement.[48]

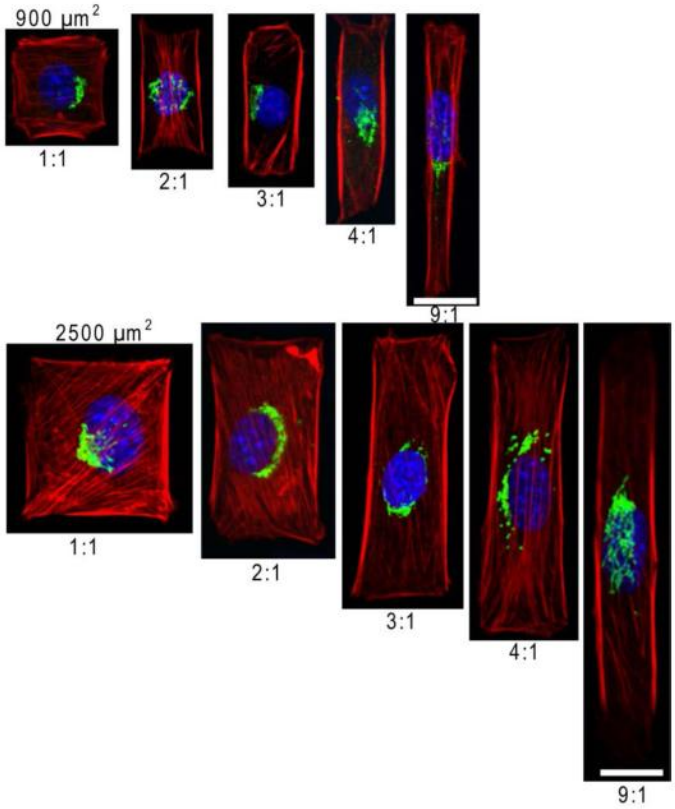

Figure 9. Cell shape and spreading area affect nuclear morphology. Actin filaments (*red*), Golgi (*green*) and nuclei (*blue*). NIH 3T3 cells were confined in individual adhesive island with area of 900 or 2500 μm2 with aspect ratios varying from 1 to 9. The scale bar represents 20 μm Figure from reference[46]

Differentiation – Osterix (OSX) and alizarin red

As mentioned previously, stem cells may differentiate into several types of cells including adipocytes, chondrocytes and osteocytes (Figure 10).[26] Osterix (OSX) and Alizarin red staining were used to probe the extent of differentiation into osteocytes.

OSX is a bone transcription factor which when activated becomes localized in the nucleus.[49] It is necessary for the differentiation of preosteoblasts into the mature functioning osteoblasts.[50] Previous literature has shown that OSX is localized to the nucleus in osteogenic cells around day seven[50], therefore it is useful as an indicator of osteogenic differentiation of MSCs.

Alizarin red is commonly used for the detection of calcium by binding to form an insoluble calcium salt.[51] Calcification occurs at matrix vesicles present in mineralizing cartilage, which contain Ca^{2+} and inorganic phosphate for the formation of hydroxyapatite ($Ca_{10}(PO_4)_6(OH_2)_2$), the main inorganic component of bone.[51]

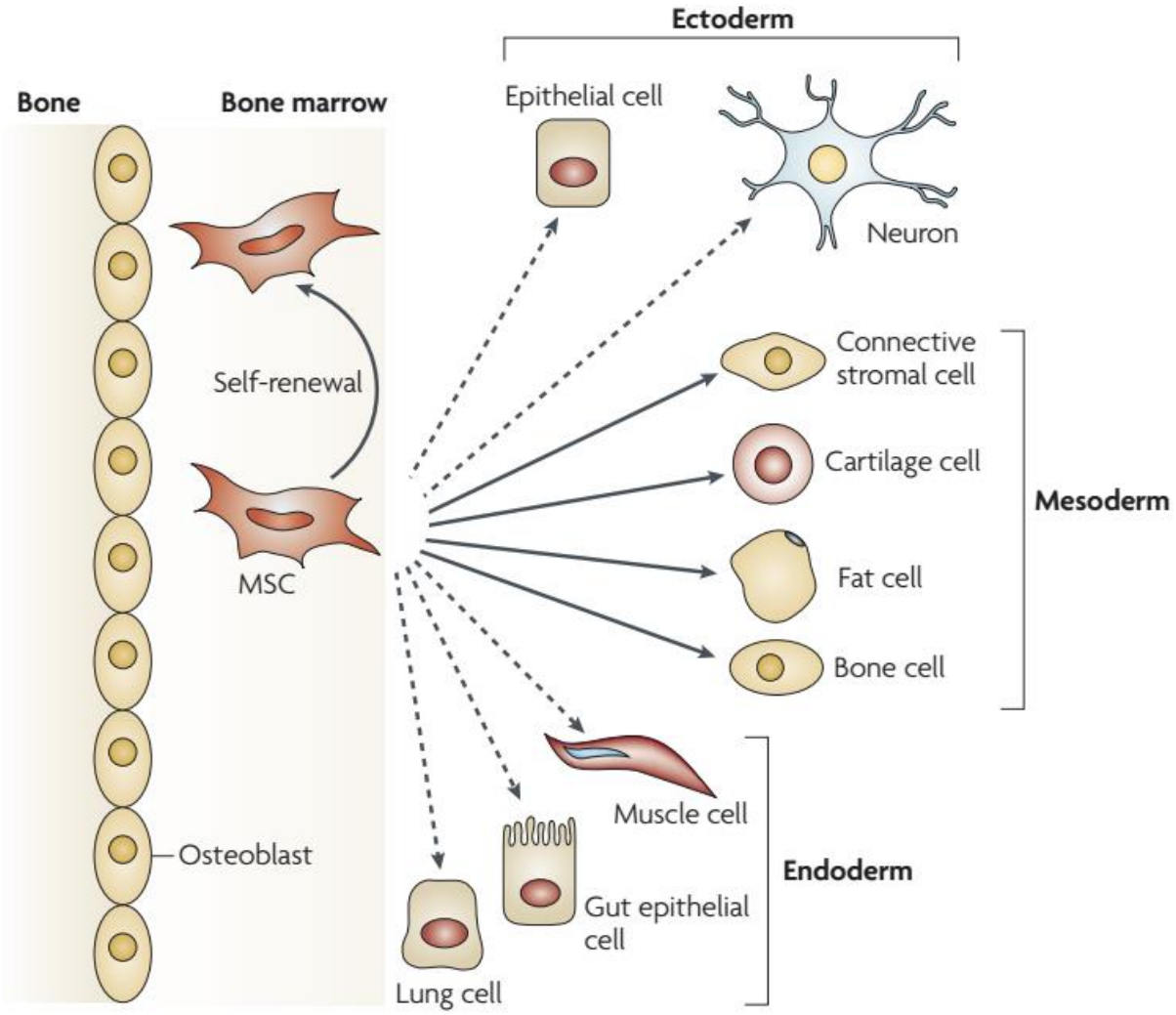

Figure 10. Mesenchymal stem cell differentiation and self renewal. Mesenchymal stem cells (MSCs) in the bone-marrow may experience self-renewal (curved arrow) or differentiate (straight, solid arrows) towards the mesodermal lineage. Differentiation into cells of other lineages (ectoderm and endoderm) is shown by dashed arrows. Figure from reference [52]

1.5.6 Stem Cell-Nanotube Interactions

Nanotubular surfaces

Previous research on stem cell-nanotube interactions have been making steady progress over the last ten years. However, a mismatch in the size, treatment and quality of nanotubes between different research groups leads to sometimes contradicting results. This calls out for more comprehensive studies to clarify incongruities in the literature. For example, Park *et al.* [53]

investigated TiO_2 nanotubes with defined diameters between 15 and 100 nm and showed that cell adhesion and spreading were severely impaired on nanotube layers with a tube diameter larger than 50 nm, with increased programmed cell death. Cell adhesion, proliferation and spreading was most improved on the 30 nm and 15 nm surfaces (Figure 11).[54] Oh *et al.*[55] showed that altering the dimensions of TiO_2 nanotubes affects hMSC adhesion and differentiation into osteoblasts. In this study, small (~30-nm diameter) nanotubes promoted adhesion without noticeable differentiation, and larger (~70- to 100-nm diameter) nanotubes elicited a tenfold increase in stem cell elongation which induced cytoskeletal stress and selective differentiation into osteoblast-like cells.[56] Park and colleagues[57] demonstrated that 15 nm nanotubes provide a substantially stronger stimulation of differentiation of rat mesenchymal cells to endothelial cells and smooth muscle cells than 70-100 nm nanotubes, with high rates of apoptosis being seen on 100 nm nanotubes. Furthermore, they found that endothelial cell adhesion, proliferation, and motility were several-fold higher on 15 nm compared to 100 nm nanotubes. Yu and colleagues[58] found that nanotube diameters of 20– 70 nm provided an effective length scale for cell adhesion, and mineralization, with them being severely impaired on nanotubes with 100–120 nm diameter. They also noted that the cell proliferation increased with increasing nanotube size.[58]

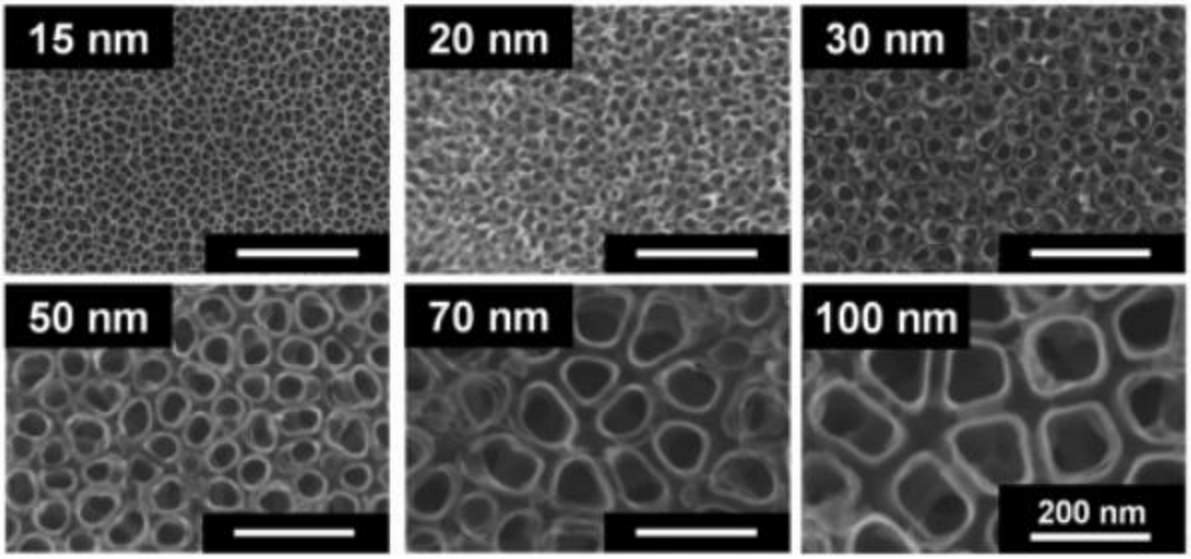

Figure 11. Surface of layers of self-aligned TiO_2 nanotubes with different diameters. Self-assembled layers of vertically oriented TiO_2 nanotubes were generated by anodizing titanium sheets. SEM images show highly ordered nanotubes of six different pore sizes between 15 and 100 nm created by controlling potentials ranging from 1 to 20 V. Figure from reference [54]

Nanoscale Symmetry and Disorder

The importance of nanoscale disorder has been demonstrated by Dalby *et al.*, who showed that nanoscale disorder can stimulate hMSCs to produce bone mineral *in vitro*, in the absence of osteogenic supplements, with similar efficiency to that of cells cultured with osteogenic media (Figure 12). In contrast, highly ordered nanotopographies produced low to negligible cellular adhesion and osteoblastic differentiation. This enhanced differentiation is the first study to suggest that the use of disorder may be an effective strategy in generating control over MSCs for regenerative medicine and tissue engineering. Despite this important finding, no previous work has addressed this aspect on nanotubular titanium surfaces.

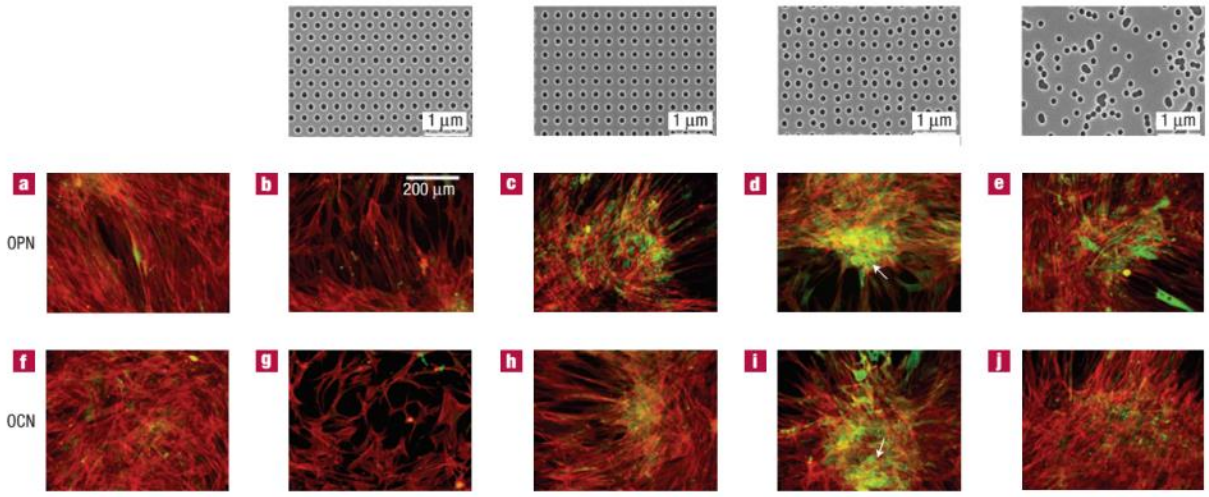

Figure 12. Osteopontin (OPN) and Osteocalcin (OCN) staining of osteoprogenitor cells after 21 days of culture. All nanotopographies have 120-nm-diameter pits (100 nm deep, absolute or average 300 nm centre–centre spacing) with hexagonal, square, displaced square 50 (±50 nm from true centre) and random placements. a–j, Osteoprogenitors cultured on the control (a,f) Actin = red, OPN/OCN = green. Figure from reference[12]

CHAPTER 2: MATERIALS AND METHODS

2.1 Substrates preparation and characterization

Nanotube Formation

Titanium foil, 0.127mm (0.005in) thick, (99.99+% purity, Alfa Aesar) were used for producing nanotubular surfaces. Highly ordered self-assembled TiO_2 nanotubes of different diameters were formed by varying the experimental parameters of anodization carried out by using an electrochemical cell with a two-electrode configuration (Figure 13). Platinum foil served as a counter electrode. Electrochemical treatments were carried out according to previous reported work[59] in 0.3 wt% ammonium fluoride, 2% wt H_2O in ethylene glycol with applied potentials from 20 V up to 60 V for 5 min to 1h at ambient temperatures. All electrolytes were prepared from reagent grade chemicals and deionized water.

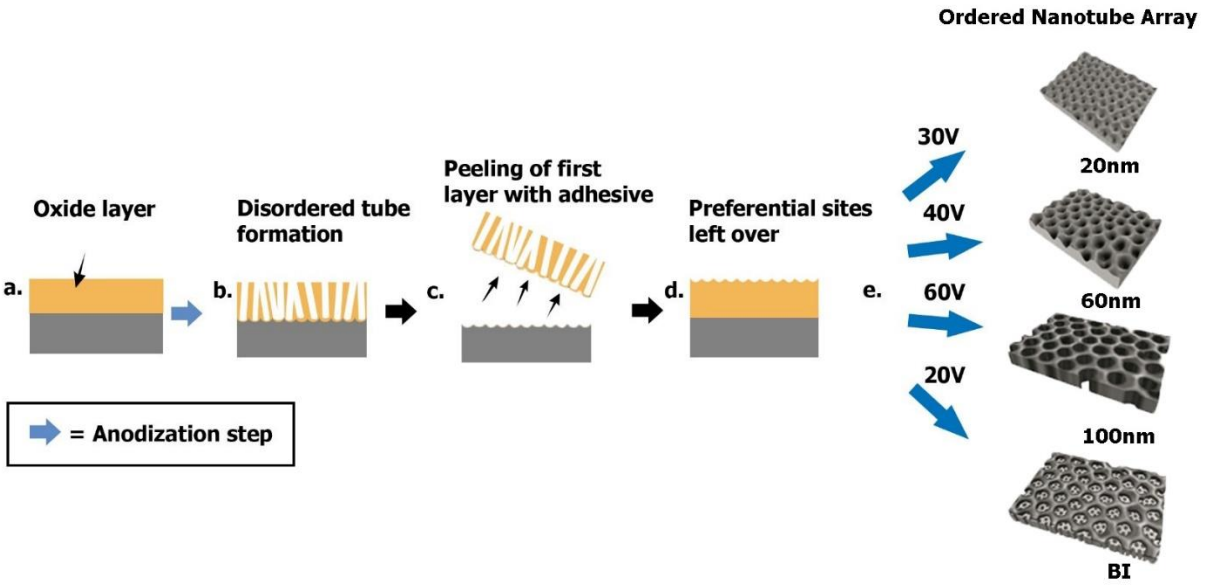

Figure 13. Schematic for a two-step anodization of titanium nanotubes. (a) Titanium surface with native oxide layer. (b) First anodization step leads to formation of disordered nanotubes. (c) First layer of nanotubes is peeled off with adhesive, leaving preferential sites (d) where the tube bottoms were previously. (e) shows differential conditions leading to semiordered nanotube formation. All conditions were the same between first and second anodizations except for BI, which was anodized at 60V first, and 20V successively.

Table 1. Formation conditions for different nanotubular surfaces on titanium. After the 1st anodization, nanotube layers were peeled off with adhesive before successive anodization.

	20 nm	60 nm	100 nm	Biomimetic
Voltage	30V	40V	60V	60V, then 20V
Time (1st Anodization)	60 min	45 min	30 min	30 min
Time (2nd Anodization)	5 min	25 min	10 min	20 min

Morphological analysis

Scanning Electron Microscopy

The morphology of the different nanotube topographies was investigated using a scanning electron microscope (SEM, JEOL 6610LV SEM) at 45,000 X magnification. The same instrument was used to image the interactions between the HMSC filopodia and nanotubes, after gold

sputtering to a thickness of 5 nm by a Q105R Rotary-Pumped Sputter Coater (Quorum) prior to imaging.

Atomic Force Microscopy (AFM)

Atomic Force Microscopy (AFM) was used to visualize the 3D nanotopography of the samples. Images were acquired using the AFM module of the alpha300 RSA system (WITec, Germany). Analysis of the sample topography was acquired using the non-contact (AC) mode with area analyzed size of 2.5μm x 2.5μm.

Nearest Neighbor Analysis

Nearest neighbor analysis was carried out on SEM images with ImageJ/Fiji software (NIH) via the nearest neighbor distance plugin. Spreadsheets were created from the software and analyzed with Origin (OriginLab, Northampton, MA).

Voronoi Analysis

Voronoi analysis was carried out on SEM images with ImageJ/Fiji software (NIH) via the nearest Voronoi analysis plugin, after utilizing the software to ascertain the centroids of each nanotube. Images were further thresholded in ImageJ and the Voronoi cell areas were recorded. Spreadsheets were created from the software and analyzed with Origin (OriginLab, Northampton, MA). The same images with Voronoi cells were run through a custom cellprofiler pipeline to delineate the Voronoi defects per image.

Wall Thickness

Wall Thickness analysis was carried out on SEM images and measured through ImageJ/Fiji software (NIH) through the line measurement tool. Lines were drawn through sets of nanotubes and recorded through the region of interest (ROI) manager. Spreadsheets were created from this data and the distances between the nanotubes were analyzed with Origin (OriginLab, Northampton, MA).

Contact angle Analysis

The water contact angle was measured with a VCA Optima Surface Analysis System (AST Products Inc., USA). A drop of distilled water (1 ul) was ejected through a micro syringe (Hamilton Company, USA). Outline of key points of the droplet was performed manually to ensure accuracy prior to automated measurement of the angle. Three droplets were measured per samples and performed in triplicate.

2.2. Cell Cultures

Bone-marrow derived human mesenchymal cells

Bone-marrow derived human mesenchymal cells (BM-hMSCs, RoosterBio, USA) were expanded in DMEM + 4.5 g/L glucose, L-glutamine (Corning, USA) supplemented with 10% fetal bovine serum (GIBCO, USA) and 20 U ml-1 penicillin and streptomycin (GIBCO, USA) at 37°C, 5% CO_2 in a water jacketed incubator. Cells were detached with 1x TrypLE Express (ThermoFisher, USA), incubated at 37°C, centrifuged at 200 g for 8 min and reconstituted in fresh culture media.

Cell Proliferation, Area, Form Factor and Nuclei Elongation

hMSCs were plated on titanium surfaces with cell densities of 4500/cm^2. Images were taken of each sample following a 5x5 grid on an epifluorescent microscope (Axio Observer Z1, Zeiss, Germany), covering an area of approximately 4200μm x 3200μm. Cell growth was analyzed by counting cells 6 h, 24 h, and 48 h after cell plating. Cell area, form factor and nuclei elongation were analyzed through a custom Cellprofiler pipeline. Experiments were performed three times in triplicate.

Focal adhesion complex visualization

After incubation at 6, 24 and 48 hours, cells were fixed with 4%-PFA and stained with Rhodamine Red Phalloidin (ThermoFisher, USA), Hoechst 33342 (ThermoFisher, USA), 1:400 mouse monoclonal Anti-vinculin (Sigma, USA) and Goat anti-Mouse IgG conjugated to AlexaFluor 488 (ThermoFisher, USA) as the secondary antibody at a dilution of 1:100. Multi-channel images were captured with an AxioObserver.Z1 inverted microscope (Zeiss, Germany).

Osteogenic differentiation

The expression of Osterix (OSX) using epifluorescence was utilized to probe extent of osteogenic differentiation. Cells were seeded at a density of 4500/cm^2 and incubated for 7 days, and subsequently fixed and permeabilized with 4% PFA and 0.5% Triton TX-100. Osterix was visualized using the mouse monoclonal OSX antibody preconjugated to AlexaFluor 647 (Santa Cruz Biotech, USA). Cells were imaged with a 20x Plan-Apo Objective (N.A.=0.95, Zeiss, Germany) attached to a AxioObserver.Z1 (Zeiss, Germany) and subsequently processed with a

custom pipeline in CellProfiler. Alizarin red staining was performed by gently shaking the plates with the stain at room temperature for 20 minutes on cells which had been growing for 28 days.

CHAPTER 3: RESULTS

3.1.1 Nanotubular spatial statistics

Semiordered TiO_2 nanotubes were produced by a two-step anodization process in ethylene glycol with applied potentials from 20V up to 60V for 5 min to 1h at ambient temperatures (Figure 13). After the initial anodization step, adhesive tape was used to remove the first layer of nanotubes, creating favorable nucleation sites (Figure 13) for the second anodization that produced nanotubes with different diameter (Figures 14-15). The biomimetic surface was created by varying the voltage in between the first and second anodizations. All size characterization for the surfaces was determined by exploiting a JEOL 6610LV SEM at 45,000 X magnification, as described in the experimental section.

Figure 16 shows the diameter distribution of the different nanotubular surfaces, that we classified and labelled according to their average diameter, ie small (20 nm), medium (60 nm) and large (100 nm). In addition, the size distribution displays a significant size overlap between the small BI (BI 20) and large BI (BI 120) with the conventional 20 nm and 100 nm nanotubes. We will refer to the conditions by their nanometer sizes (20 nm, 60 nm, 100 nm, BI 20, BI 120) from this point forward.

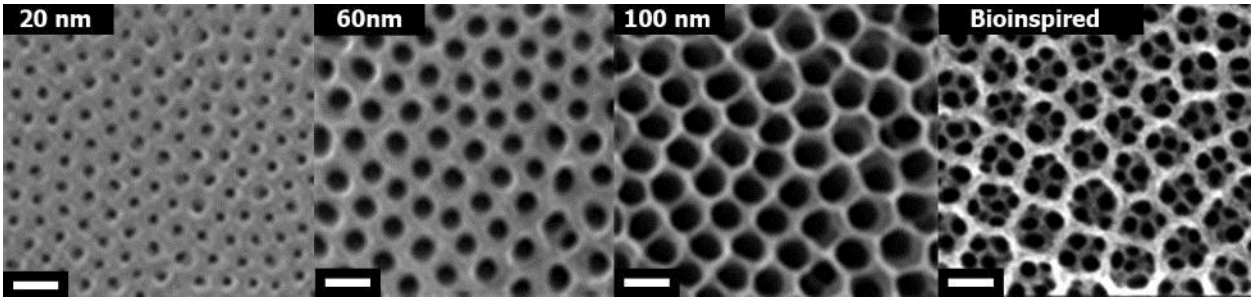

Figure 14. SEM top-views of the nanotubular layers of different tube diameters. Nanotubes were formed by anodization of titanium in 0.3%NH_4F/2%H_2O/ethylene glycol at potentials between 20V and 60V at 45,000 X magnification. Scale bar = 100 nm. Biomimetic nanotubes mimic the nanostructure of some diatom exoskeletons, and are created through a two-step anodization process with changing voltage points.

3.1.2 Wall Thickness

The wall thickness was characterized (Table 2) by image analysis of the micrographs obtained by using a JEOL 6610LV SEM at 45,000 X magnification. It is shown that the wall thickness decreases from the 20 nm to the 100 nm nanotubes, but notably differ between the BI 20 surface and the 20 nm surface. The 20 nm wall thickness averages in fact 55 nm while the BI 20 averages 24 nm.

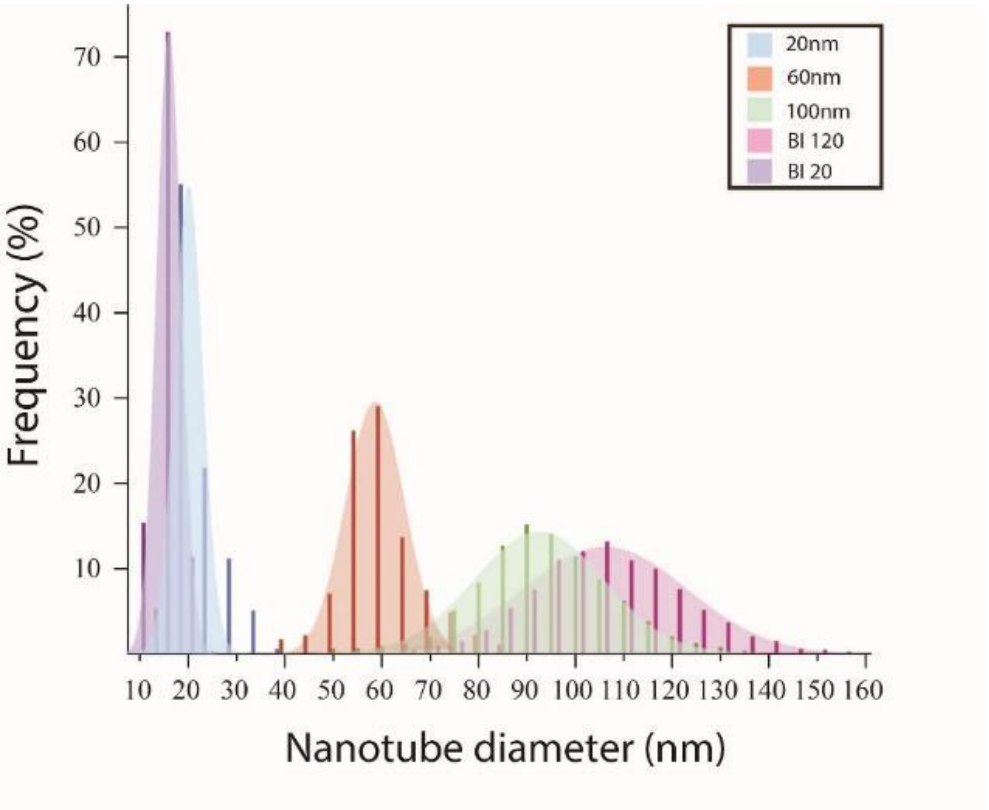

Figure 15. Nanotube diameter distributions for separate conditions. 20 nm and BI 20 have largely overlapping distributions on the lower end while 100 nm and BI 120 have mostly comparable distributions on the large end of the spectrum. 60 nm nanotubes lie in between the two extremes.

Table 2. Wall thickness of nanotubes measured from SEM images. Of the regular nanotube sets, the 20 nm nanotubular surface has the largest wall thickness, and the 100 nm surface has the thinnest walls. In the biomimetic surface both BI 20 and BI 120 show thinner walls.

Condition	20 nm	60 nm	100 nm	BI 120	BI 20
Wall Thickness [nm]	55±14	46±12	32±9	35±10	24±7

3.1.3 Atomic Force Microscopy

Additionally, atomic force microscopy was carried out on the different sets of nanotubes (Figure 16) using the AFM module of the alpha300 RSA system (WITec). This analysis served as a secondary verification to the nanotubular sizes. Moreover, the non-contact (AC) mode revealed particularly that the depth of the BI surface from the BI 120 to the BI 20 is approximately 30-40nm in height.

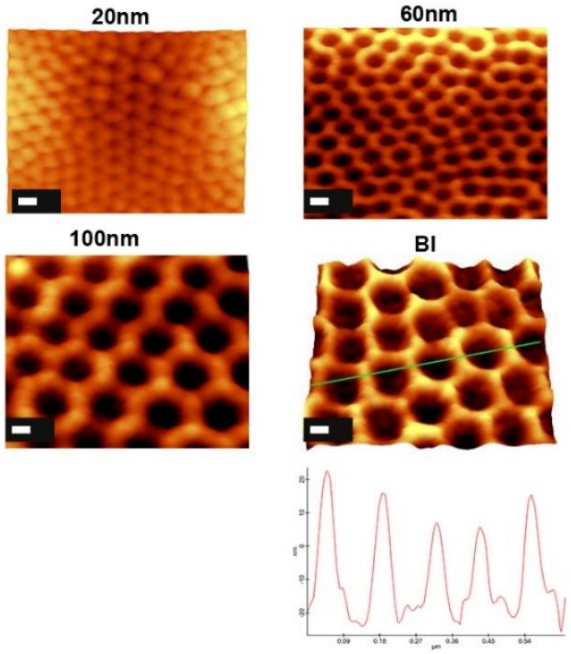

Figure 16. Atomic force microscopy images of the different sets of nanotubes. Depth of the BI 120 surface to the lower BI 20 lumen was measured to be 40nm. Scale bar = 50nm

3.1.4 Contact Angle Analysis

Contact angle analysis (Figure 17, Table 3) was performed on nanotubular samples and it was found that the hydrophilicity increases with increasing nanotube diameter. Interestingly the BI surface was more hydrophobic, displaying contact angles similar to the 20 nm condition.

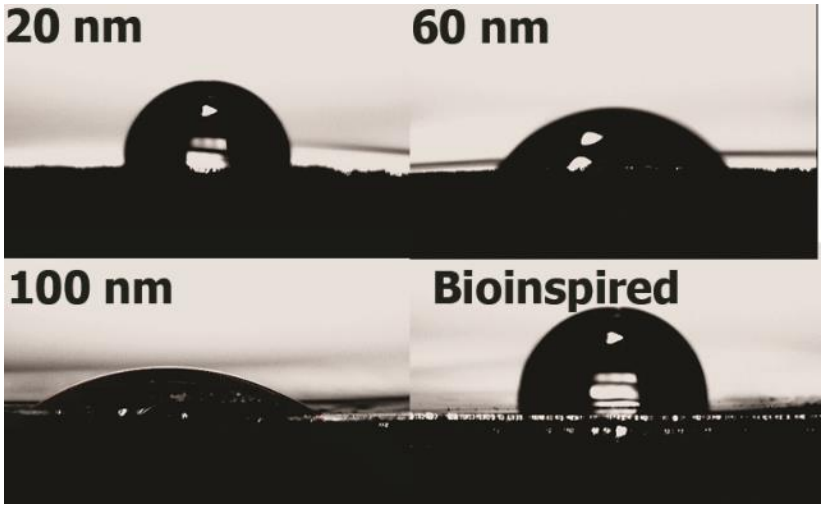

Figure 17. Contact angle analysis of the different nanotube conditions. The BI condition behaved like the 20 nm condition, with contact angles over 80 degrees, denoting a hydrophobic character, while the 60 nm and 100 nm showed more hydrophilic response.

Table 3. Contact angle values for differential nanotubular conditions

Condition	20 nm	60 nm	100 nm	BI
Contact Angle	81±4	58±7	25±3	85±2

3.1.5 Nearest Neighbor and Voronoi Analysis

Nearest neighbor distance and Voronoi analysis was performed (Figure 18) and compared to expected ordered and random models generated by ImageJ software. The perfectly ordered samples display a perfectly vertical distribution with a mean of 1, and the random samples tend to have regions of closer nucleation which shifts the mean to a lower value. In the nanotubular samples the means are centred at or near 1 with distributions which are wider than the perfectly ordered simulation. It can be seen that the nearest neighbor distance (Table 4) increases from 20 nm condition to the 60 nm to the 100 nm condition, with average values of 65 nm, 88 nm and 109 nm respectively. The BI 120 surface shares similar NND to the 100 nm condition, displaying a mean of 118 nm and the BI 20 NND is indeed also a lower value at 44 nm. Additional local Voronoi analysis (Figure 19) with BI 120 masks superimposed on the BI 20 and 20 nm surfaces showed that even measuring order within the larger nanotubes showed that the BI 20 surface's small nanotubes were more disordered than the 20 nm nanotubes.

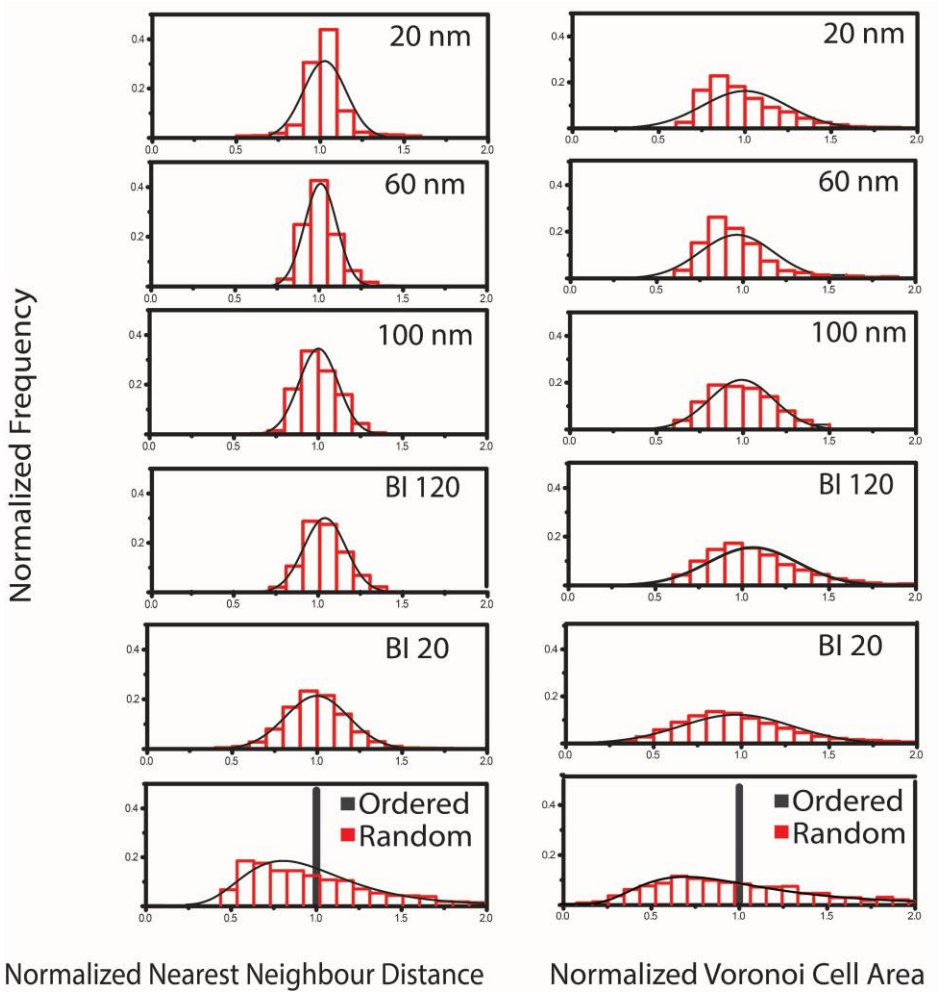

Figure 18. Normalized nearest neighbor distance and Voronoi cell area compared to expected perfectly ordered and random (disordered) computer generated models. Nanotube ordering is neither perfectly ordered nor disordered, thus termed semiordered. BI surface tends to be closer to disorder than 20 nm, 60 nm or 100 nm surfaces.

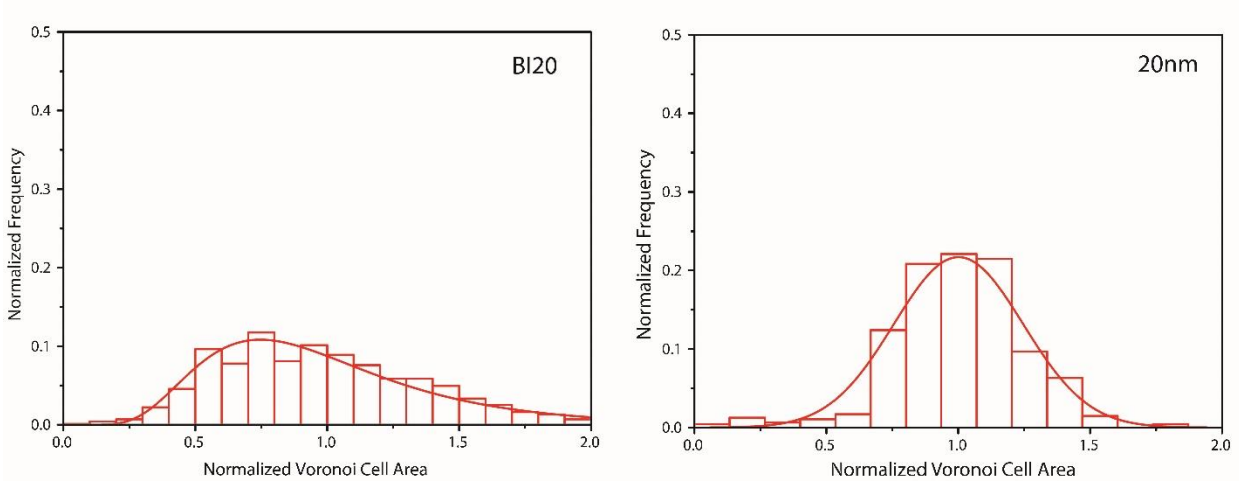

Figure 19. Local innertube order between BI 20 and 20 nm surfaces. A mask was generated to simulate the surrounding tubes of the BI surface and superimposed on both the BI 20 and the 20 nm surfaces. The local order of the smaller tubes within each of the larger tubes was measured using Voronoi cell area. This figure shows that the disorder is still present in the local regions, ie the smaller tubes nucleate in a disordered fashion within the larger tubes.

Table 4. Nearest neighbor distance as a function of nanotubular layer diameter. 100 nm NND is comparable to BI 120 whilst BI 20 is significantly different from its 20 nm counterpart.

Condition	20 nm	60 nm	100 nm	BI 120	BI 20
Nearest Neighbor distance	65±9	88±8	109±12	118±18	44±8

3.1.6 Voronoi Defects

The Voronoi defects were also measured as a function of nanotubular layer diameter through ImageJ software (Figure 20, Table 5). Voronoi defects were defined as the proportion of Voronoi cells which deviated from the ideal hexagonal spacing structure which allows for perfectly ordered and efficient packing. It was found that the Voronoi defects for the nanotubes were roughly centred at 44%-49% with the 60 nm condition having the least Voronoi defects. The BI condition had larger percentages of Voronoi defects, with the BI 120 having a mean of 54% and BI 20 having a mean of 68%.

Table 5. Voronoi defects as a function of nanotubular layer diameter. Ideal Voronoi shapes have 6 sides (each side correlates to one neighbor), as this is the most efficient distribution of nearest neighbors; those which deviate are considered Voronoi defects, which give a measurement of distance from the ideal ordered spacing of nanotubes. BI 20 is closest to the random (disordered) distribution whereas all the other conditions hover around a 50% ratio from the ideal.

Condition	20 nm	60 nm	100 nm	BI 120	BI 20	Random	Ordered
Voronoi Defects (%)	49±7	44±3	49±5	54±6	68±3	75±3	0

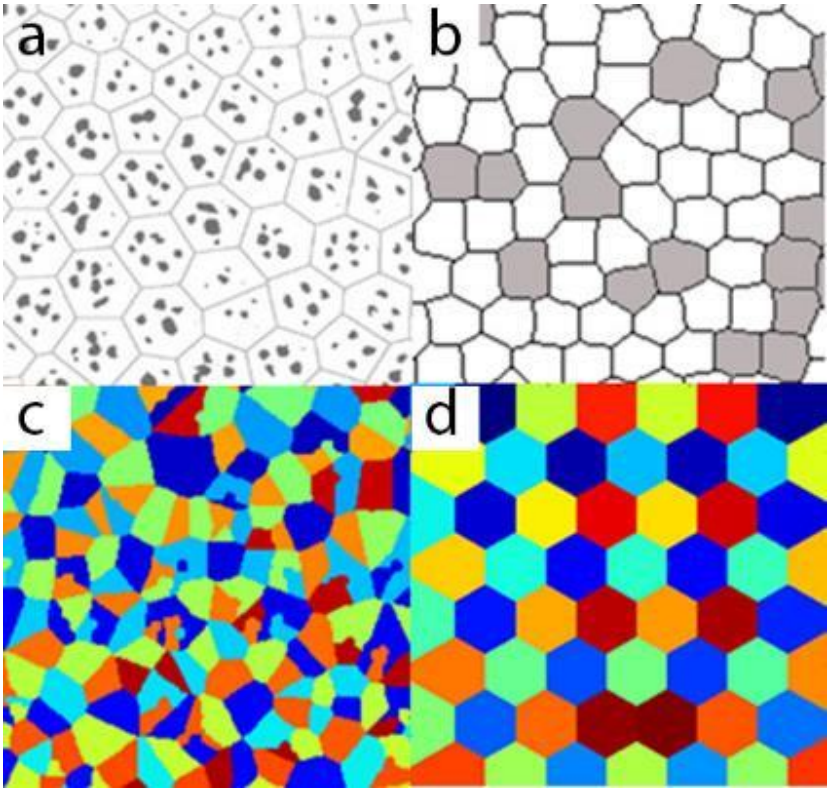

Figure 20. Voronoi defect example images. a) overlay of the Voronoi areas of BI 120 over BI 20 b) shaded regions indicate Voronoi defects. c) example of Voronoi shapes of random distribution d) example of Voronoi shape of a perfectly ordered surface.

3.1.7 Stem Cell Proliferation

Human mesenchymal stem cell proliferation was measured over three time points of 6 h, 24 h and 48 h (Figure 21) for 4 nanotubular conditions. It can be seen that in the 6 h time point notably the 20 nm condition was outperformed by the other conditions in terms of proliferation. In the 24 h timepoint the 20 nm condition and BI outperform the larger nanotubes. Finally, in the 48 h timepoint, the BI outperforms the 20 nm condition, followed by the larger nanotubular conditions. Furthermore, the average number of cells per condition actually saw a decrease from 6 h to 48 h in the 60 nm and 100 nm conditions, which indicates apoptosis as indicated by previous literature which saw an increase in apoptotic cells in larger nanotube size ranges.[57] Interestingly the 20 nm condition saw a more rapid increase in growth compared to BI, however by 48 h the cellular proliferation was still not as numerous.

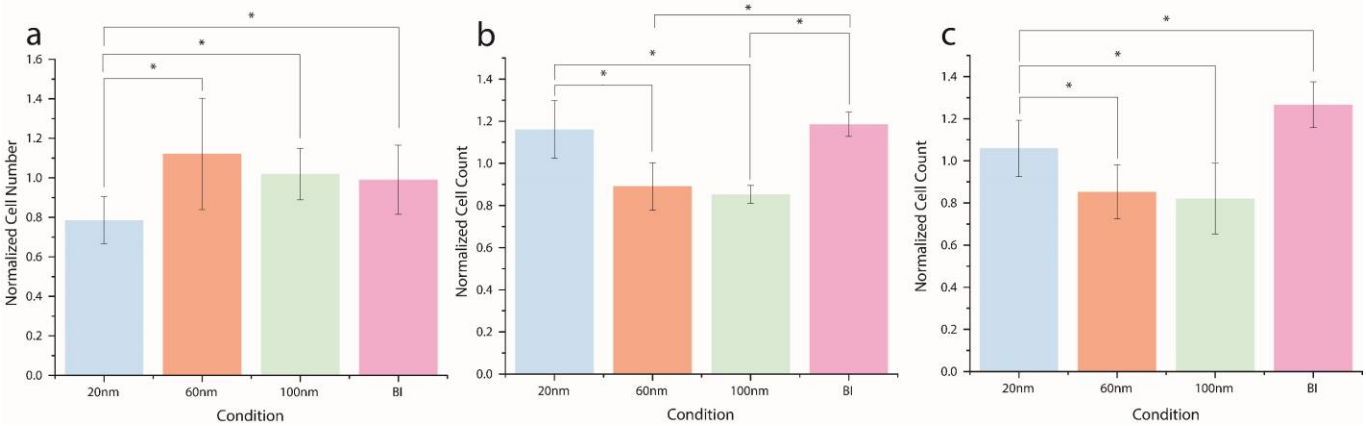

Figure 21. Cell proliferation counts for differential timepoints. a) 6 h timepoint. The 20 nm condition underperformed the other conditions at 6 h. b) 24 h timepoint. The 20 nm and BI conditions start outperforming the 60 nm and 100 nm conditions at 24 h. c) 48 h timepoint. The BI condition outperforms the 20 nm condition at 48 h. *($p < 0.05$)

Table 6. Cell proliferation and growth change. This graph shows the average number of cells per condition and the growth change after 48 h. The 20 nm and BI surfaces showed increased growth whereas the 60 nm and 100 nm surfaces showed decreased growth.

	6 h		24 h		48 h		
Condition	Avg cells	+/-	Avg cells	+/-	Avg cells	+/-	48 h Growth %
20 nm	119.0	29.7	161.2	36.6	166.7	25.3	40.1
60 nm	156.4	41.5	142.2	23.9	126.8	15.2	-18.9
100 nm	157.0	64.2	148.0	44.3	119.1	20.0	-24.1
BI	153.1	73.6	173.2	44.4	195.4	19.0	27.6

3.2.1 Cell Spreading and Morphology

Cell area and form factor were analyzed through a custom Cellprofiler pipeline (Figures 22 and 23), a form factor (calculated as $4*\pi*\text{Area}/\text{Perimeter}^2$) of 0 represents a linear cell and a form factor of 1 represents a circular cell. Over the 6 h timepoint, it can be seen that the areas of the different conditions begin quite similarly. As the time point progresses to 24 h the 20 nm and BI areas gradually increase while the 60 nm and 100 nm areas do not. As 48 h is reached it is very clear that the 20 nm and BI conditions outperform the 60 nm and 100 nm conditions in terms of area. In fact, the 60 nm and 100 nm conditions actually decrease in area at 48 h. In terms of form factor, cells at 6 h perform similarly, in that they begin neither elongated nor spherical across all conditions. By 24 h, the 60 nm and 100 nm conditions present cells which begin gravitating towards spherical form factor with the 20 nm and BI present opposing trends towards elongation. At 48 h, both the 60 nm and 100 nm conditions display trends towards elongation while the BI condition displays increased elongation compared to all other conditions. As a qualitative measure the numbers of elongated, multipolar and spherical cells were counted over all samples at 48 h and

presented as a percentage (Figure 23). It was found that the 20 nm and BI conditions have a much greater number of elongated cells and conversely the spherical cells were much more widespread in the 60 nm and 100 nm conditions.

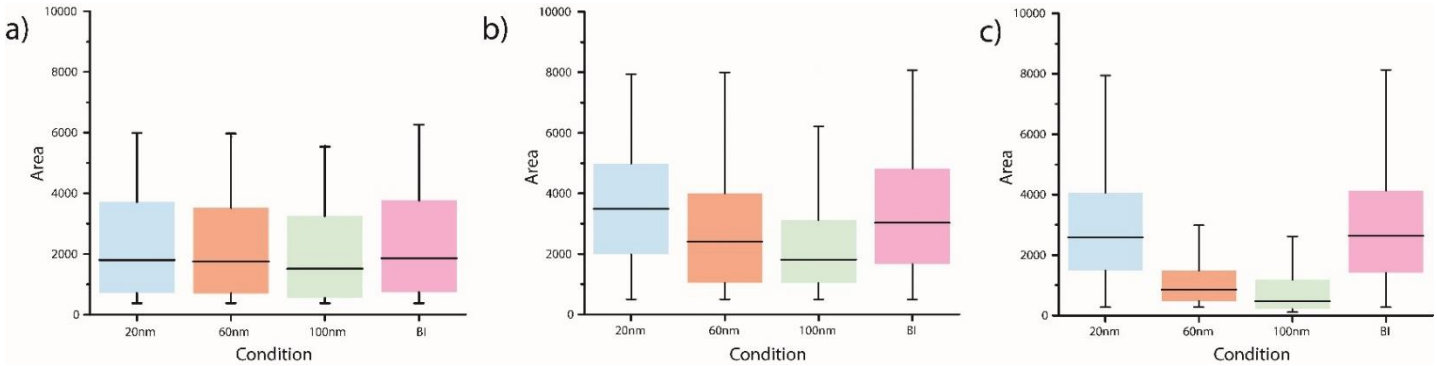

Figure 22. Box plots of cell area for differential timepoints. a) 6 h timepoint. Cells show roughly the same cell area over all conditions at 6 h. b) 24 h timepoint. 20 nm and BI conditions show distribution towards larger area than the 60 nm and 100 nm timepoints. c) 48 h condition. By this point the 20 nm and BI conditions clearly outperform the 60 nm and 100 nm conditions, which have decreased in size.

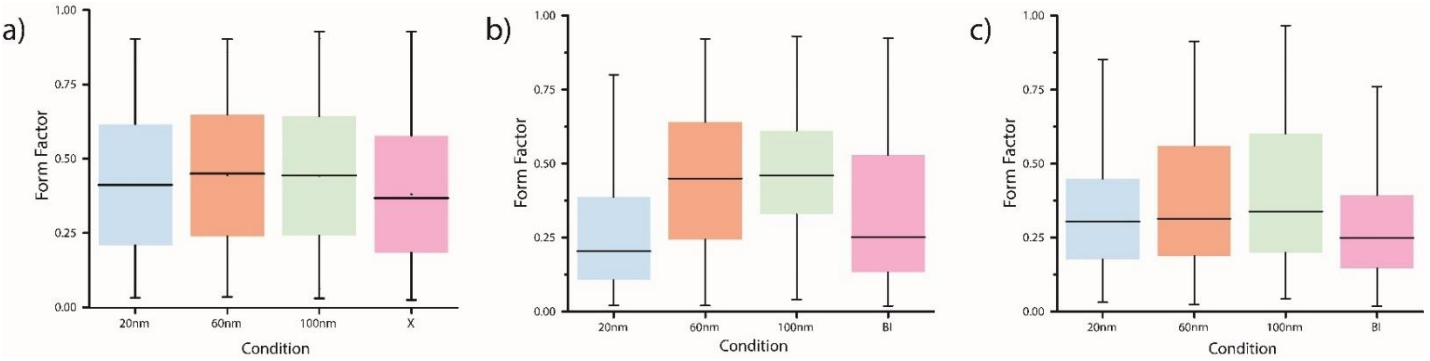

Figure 23. Box plots of form factor calculations of stem cells on nanotubular titanium for differential timepoints. A form factor (calculated as $4*\pi*Area/Perimeter^2$) of 0 represents a linear cell and a form factor of 1 represents a circular cell. a) 6 h timepoint. Cells are roughly similar in shape along all conditions b) 24 h timepoint. 20 nm and BI conditions start showing increased distribution towards elongation and 60 nm and 100 nm conditions start showing increased distribution towards spherical morphology. c) 48 h timepoint. Cells in the BI condition show a further increase in distribution towards linearity.

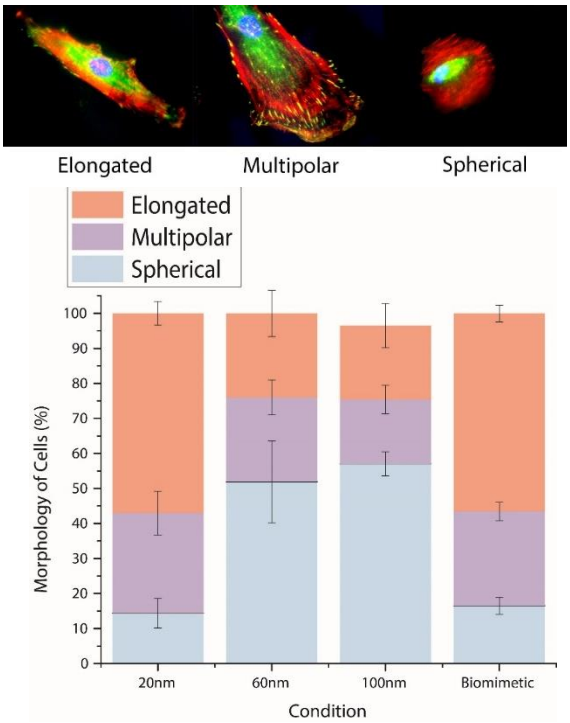

Figure 24. Cell morphology of cells in culture for 48 h. The 20 nm and BI conditions show increased elongation and multipolarity of cells and the 60 nm and 100 nm conditions show increased spherical morphology after 48 h.

3.2.2 Focal Adhesion Analysis

Focal adhesion analysis was carried out on cells stained with Hoescht nuclear stain, actin (Rhodamine Red Phalloidin) and vinculin (AlexaFluor 488) and images were captured with an AxioObserver.Z1 inverted microscope. Focal adhesion lengths and number/cell were measured for each sample condition at 48 h (Figure 25, Tables 7 and 8). The 48 h timepoint was chosen to give cells time to spread and focal adhesions to mature. It is clear after 48 h that the 20 nm and BI surfaces show many larger focal adhesions (>5 microns) and that the 60 nm shows many medium-sized focal adhesions (2-4 microns), but lack larger adhesions. Finally, the 100 nm condition shows mostly adhesions <2 microns in size. The number of focal adhesions/cell at 48 h show that the BI surface has a significantly larger number of focal adhesions/cell, followed by 20 nm condition, which is then followed by both the 60 nm and 100 nm conditions which have the least.

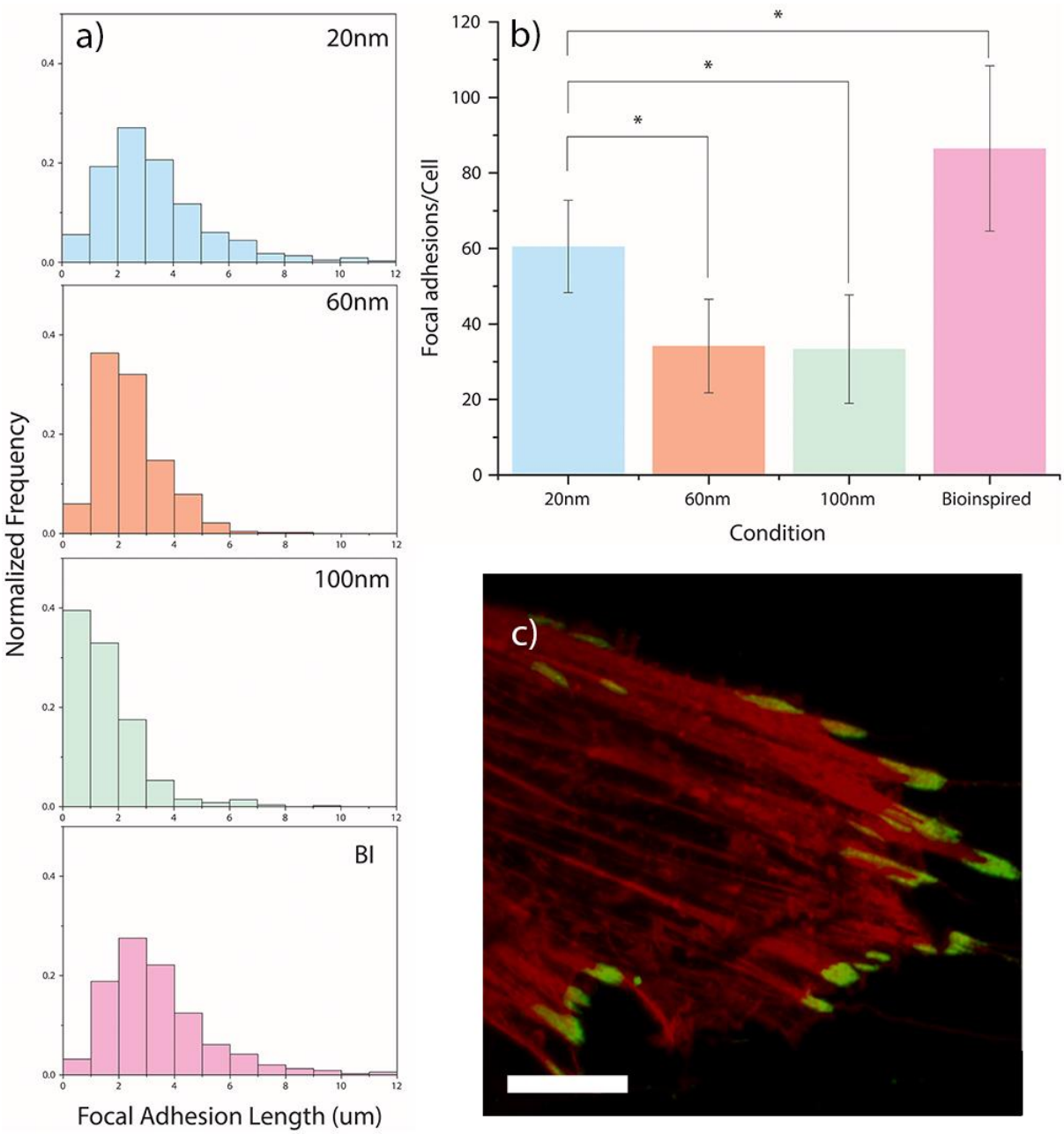

Figure 25. Focal adhesion analytics for differential nanotube morphologies. a) Distributions of focal adhesion lengths for nanotubular morphologies. 20 nm and BI show larger focal adhesions than 60 nm and 100 nm conditions. b) Focal adhesions per cell. BI shows more focal adhesions/cell than 20 nm. Both 20 nm and BI show more focal adhesions then 60 nm and 100 nm conditions. c) High resolution fluorescence airyscanning image of focal adhesions (green protrusions at cellular edge) on a mesenchymal stem cell. Green = vinculin, red = actin. Scale bar = 10 μm. *($p < 0.05$)

Table 7. Average focal adhesion lengths. This table shows the average focal adhesion lengths for the bottom 90% of focal adhesions for each condition, which include nascent adhesions, focal complexes and focal adhesions (but not fibrillar adhesions). 20 nm and BI have larger focal adhesions than 60 nm and 100 nm conditions.

Condition	20 nm	60 nm	100 nm	BI
Avg Focal adhesion length (μm)	3.3±2.1	2.4±1.2	1.5±1.6	3.4±1.9

Table 8. Average focal adhesion lengths (large). This table shows the average focal adhesion lengths for the top 10% of focal adhesions for each condition, which include the largest class of focal adhesions, fibrillar adhesions. 20 nm and BI have larger fibrillar adhesions than the 60 nm and 100 nm conditions

Condition	20 nm	60 nm	100 nm	BI
Avg Focal adhesion length (μm)	7.8±1.9	5.5±1.4	4.9±.0.9	7.9±1.9

3.2.3 Nuclear Elongation

The nuclear major axis length was measured over all conditions at 48 h (Figure 26) via a custom Cellprofiler pipeline. It was found that both the 20 nm and BI conditions had significantly longer nuclei than the 60 nm and 100 nm conditions.

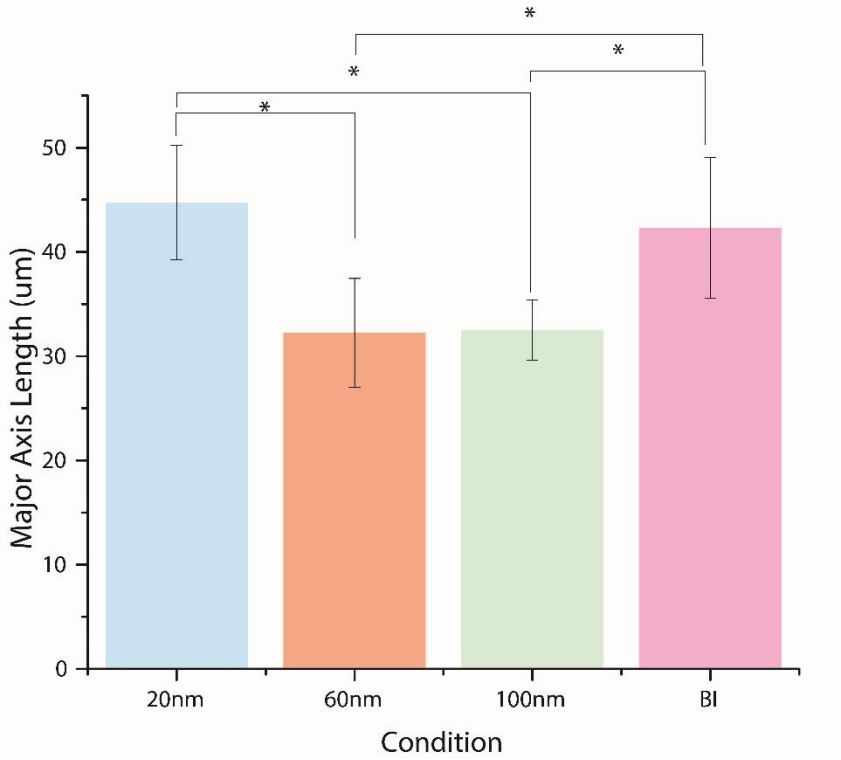

Figure 26. Nuclei major axis length for nanotubular conditions after 48 h. Nuclei were elongated on 20 nm and BI surfaces, indicating cytoskeletal stresses were transduced to the nuclei, which may effect nuclear function.[60,61] *($p < 0.05$)

3.2.4 Osteogenic Potential

The expression of locational expression of Osterix (OSX) proteins using epifluorescence was utilized to probe extent of osteogenic differentiation. At 7 days (Figure 27) the OSX was found in every condition to have localized to the nucleus. At 28 days (Figures 28 and 29) the samples were stained with Alizarin red which binds to calcium deposits found in osteogenic cells. The lightest staining was observed on the control, with sparse to no redness, followed by the 20 nm condition, the 60 nm condition, BI, and finally the darkest red appeared on the 100 nm condition, with a thick layer almost appearing black in colour.

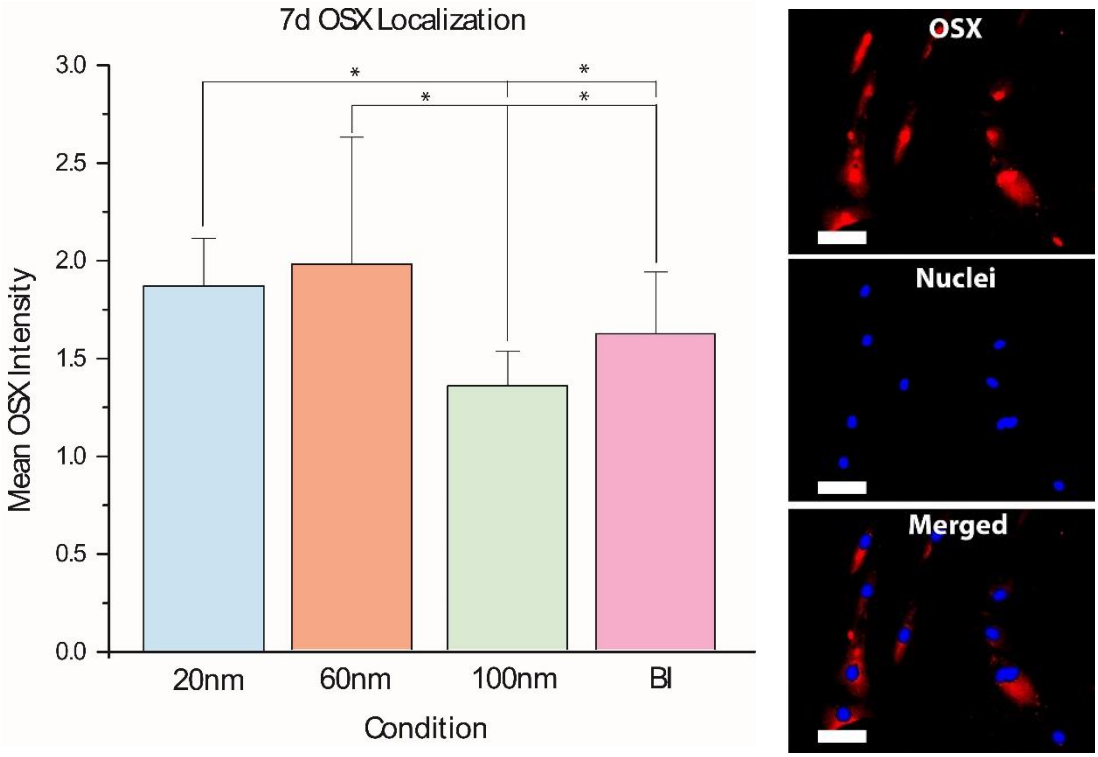

Figure 27. Osteogenic differentiation through OSX staining**.** a) Nuclear localization of osterix protein, OSX in human mesenchymal stem cells after 7 days in culture, relative to the intensity of osterix localized to the cytoplasm (represented at 1.0) OSX was shown to localize to the nucleus, which suggests osteogenic capacity for nanotubular samples. b) Example of OSX fluorescence staining and nuclear localization. Scale bar = 100 μm. *($p < 0.05$)

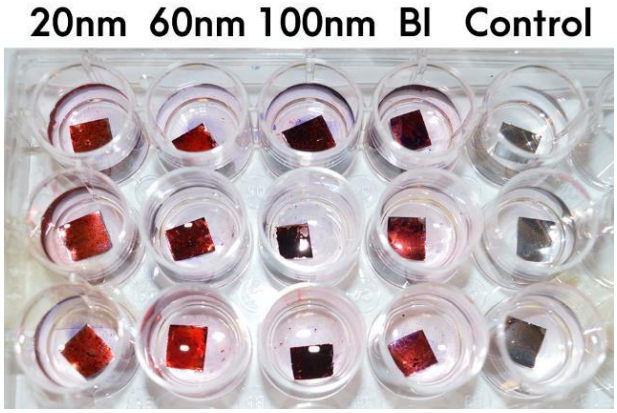

Figure 28. Alizarin red staining of nanotubular conditions. Alizarin red binds to calcium deposits found in osteogenic cells. The lightest staining was observed on the control, with sparse to no redness, followed by the 20 nm condition, the 60 nm condition, BI, and finally the darkest red appeared on the 100 nm condition, with a thick layer almost appearing black in colour.

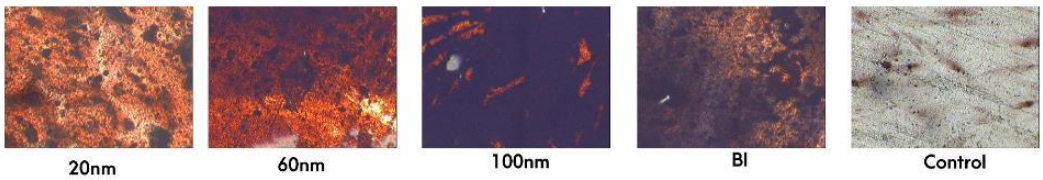

Figure 29. Optical microscope images of alizarin red stained nanotubular conditions.

3.2.5 Scanning Electron Microscopy of Filopodia

SEM was carried out on fixed cells at 24 h (Figure 30). There were filopodial interactions observed on the nanoscale, as filopodia were seen to protrude over the nanotubes, presumably with their integrin and FA complexes contacting the surface mechanically.

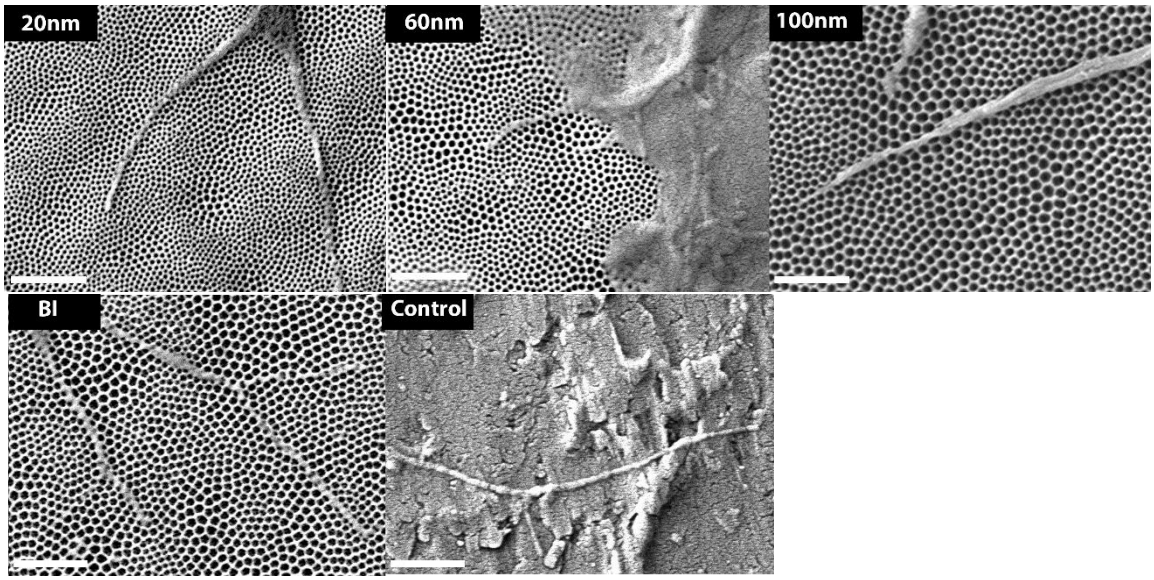

Figure 30. SEM micrographs of filopodia on nanotube conditions. Scale bar – 1 μm.

CHAPTER 4: DISCUSSION

4.1 Nanotubular Morphology and Spatial Statistics

Through a two-step anodization process, semiordered TiO_2 nanotubes were produced in ethylene glycol with applied potentials from 20 V up to 60 V at differing time scales (Table 1). After the initial anodization, an adhesive was applied to the titanium surface to remove the first layer of nanotubes, creating favorable nucleation sites for the second anodization that produces nanotubes with increased ordering. The resulting nanotubular structure was similar to those of Wang *et al.*[18], who used a similar double anodization and peeling process to produce nanotubes showing superior order (Figure 16) to single-anodized samples (Figure 11). The BI surface was formed by decreasing the voltage from the first to the second anodization, producing smaller nanotubes which seemed to nucleate within the larger initial imprints left by the peeling, creating a combinatorial surface with unique size, height and order characteristics (Figure 14). In comparison to previous studies performed with titanium nanotubes, our nanotubes are clearly more ordered and do not present the inter-tube space (empty space between nanotubes) which previous studies show (exemplified in Figure 11), which present an extra variable when delineating whether the effects seen are truly due to the nanotubes or inter-tube space.

Size characterization was validated on a JEOL 6610LV SEM at 45,000X magnification (Figure 15). There is a strong demarcation between the small (20 nm), medium (60 nm) and large (100 nm) conditions (Figure 16), as well as substantial overlap between the small BI (BI 20) and 20 nm, and large BI(BI 120) with the 100 nm nanotubes. These findings show a positive correlation between voltage and nanotube size. While lower voltages produced smaller nanotubes, higher voltages produced larger nanotubes. A voltage of 30V produced the smallest nanotubes (20 nm) and the 60V condition produced 100 nm nanotubes. A correlation was also found between time

and nanotube size, with relatively smaller tubes being produced at lower time intervals. These findings correlate to Poulomi *et al.*'s findings in their comprehensive review on titanium nanotube growth studies over the past decades.[9]

Wall thickness decreases with diameter, except for BI surface

The wall thickness was analyzed (Table 2) with the images obtained by the JEOL 6610LV SEM at 45,000 X magnification through ImageJ measurement tools. The findings show wall thickness decreasing from the 20 nm to the 100 nm nanotubes, but marked differences show between the BI 20 surface and the 20 nm surface. The 20 nm wall thickness showed an average of 55 ±14nm while the BI 20 averages 24±7nm and is a point of difference when comparing the two similarly sized nanotubes. This means that there is significantly larger titanium surface area on the 20 nm surface and significantly increased tubular surface on the BI condition which could serve in the interpretation of the cellular results on those surfaces, especially since the surface energy is known to affect adsorption of proteins beneficial to focal adhesion growth such as fibronectin and collagen, as reported by Yang and colleagues.[62] Moreover, Coyer *et al.* demonstrated that cells adhere to fibronectin nanopatterns and that integrin clustering on fibronectin islands were modulated by nanoscale ECM area, and that below a threshold area of 0.11 μm^2, no appreciable adhesive forces are generated, illustrating the importance of nanoscale adhesive surface area on cellular adhesion.[63]

BI surface has height of 40 nm between higher and lower levels

Furthermore, the AFM module of the alpha300 RSA system (WITec) was used to carry out atomic force microscopy on the different sets of nanotubes (Figure 16). The non-contact (AC) mode exposed that the depth of the 'nanovalley' from BI 120 to the BI 20 is in the 30-40 nm range. It is especially interesting to note that this is the approximate z-position of important protein

portions of the FA including integrin tails, focal adhesion kinase (FAK), paxillin, talin and vinculin, as reported by Kanchanawong *et al*.(Figure 31)[64] This specific height of the BI nanotubular wall between BI 20 and BI 120 may allow for physical mechanotransductive interactions between the nanotubular walls on the BI surface and the important signaling proteins of the FA. In particular, Carisey *et al*.[65] showed that vinculin controls the transmission of force from the cell's extracellular environment and proposed a model whereby vinculin organizes the core proteins of the FA. Those authors note that if exposed to continuous forces from their external environment (such as the vertical wall of the BI surface), "outside-in" signaling may continuously activate vinculin to switch its regulatory role in FA assembly and disassembly to a stable force-transducing connection role between the integrin-talin complex and the actin cytoskeleton, maintaining the cell shape.[65] Therefore this force transducing role may play a part in explaining the improved performance of the BI surface. Additionally the 40 nm vertical wall is a source of further surface area for the BI surface, along a third dimension which may serve a role to increase fibronectin, collagen and other important protein adsorption onto the ECM nanosurface.[62,63]

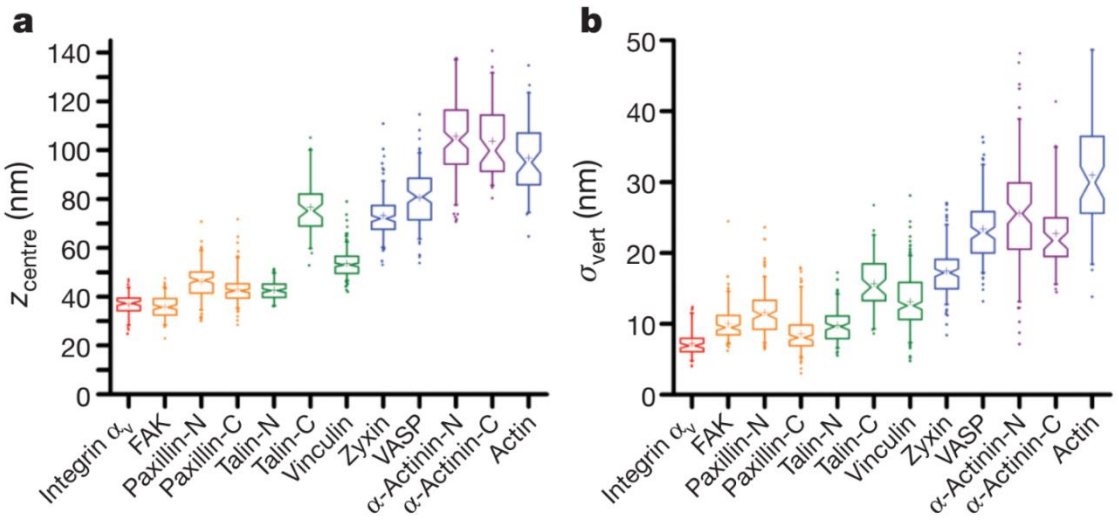

Figure 31. Peak position (zcentre)(a) and width parameter ($^{\sigma}$vert)(b) of photoactivatable fluorescent proteins fusions in focal adhesions. Notched boxes, 1st and 3rd quartiles, median and confidence interval; whiskers, 5th and 95th percentiles; +, means, outliers also shown. Figure from reference [64]

Nanotube conditions are semiordered

Nearest neighbor distance (NND) measures distance between each centroid and its nearest neighbor's centroid location, providing a measure of degree of spacing or clustering. Voronoi cell areas (VCA) are the areas of the partitioned Voronoi diagram of a surface. Voronoi "defects" refers to the cells which have greater or less than 6 edges indicating a suboptimal order. Nearest neighbor distance and Voronoi analysis was completed (Figure 18) and related to expected ordered and random models generated by ImageJ software, similar to the process used by Ratto et al. in characterizing order of surfaces.[25] The perfectly ordered samples display a perfectly vertical distribution with a mean of 1, and the random samples have a lower valued mean and a much wider range. In the nanotubular samples the means are centred at or near 1 with distributions which are wider than the perfectly ordered simulation and narrower than the random condition. Accordingly, our nanotubular surfaces are thus termed semiordered, tending towards order.but neither perfectly ordered nor disordered.

20 nm condition and BI condition display hydrophobic wetting behavior

Protein adsorption and cell adhesion have been known to affected by wetting behavior of the surface, with hydrophobic surfaces leading to improved cellular attachment, as Bauer *et al*. have shown.[66] Additionally, Oh *et al.* showed that protein aggregates settle on the nanotube surface, which affect how cells initially perceive and attach to the surface. They found that less protein aggregate was deposited on larger (100 nm) nanotubes, while more was deposited on smaller (30 nm) nanotubes.[55] Nanotubular samples had contact angle analysis (Figure 17, Table 3) studies performed and it was found that the hydrophilicity increases with increasing nanotube diameter. Interestingly the BI surface was more hydrophobic, displaying contact angles similar to the 20 nm condition.

Nearest neighbor distance increases with diameter

The nearest neighbor distance (Table 4) increases with nanotube size, with means of 65±9nm, 88±8nm and 109±12 nm for the 20 nm, 60 nm and 100 nm surfaces respectively. The BI 120 surface shares similar NND to the 100 nm condition, displaying a mean of 118±18nm and the BI 20 NND is also a lower value at 44±8nm. A difference between the 20 nm condition and the BI 20 NND values exists; the BI 20 mean values are approximately 19nm closer together.

BI surface is semiordered, but tends towards disorder

Voronoi defects were calculated against nanotube diameter (Figure 20, Table 5) and are the proportion of Voronoi cells which deviated from the ideal hexagonal spacing structure, which have 6 sides to each Voronoi cell. It was found that the mean Voronoi defects for the nanotubes varied from 44%-49% . The 60 nm condition displayed the least Voronoi defects. The BI condition displayed increased Voronoi defects, with the BI 120 having a mean of 54% and BI 20 having a mean of 68%. This can be interpreted as a result of alternating different voltages from the first

anodization to the second anodization, with the initial pores formed influencing the possible nucleation sites for the second anodization at a different voltage (and size). The relative disorder is thus another point of difference between the 20 nm condition and the BI 20 condition. Additional local Voronoi analysis (Figure 19) with 'BI 120' masks superimposed on the BI 20 and 20 nm surfaces showed that the disorder was higher on the BI 20, and that the disorder of the BI 20 surface's small nanotubes are present locally as well as globally.

4.2 Cellular Studies

By 48 h BI condition outperforms other conditions' proliferation

After 6 h, 24 h and 48 h (Figure 21), images were taken of each sample following a 5x5 grid on an epifluorescent microscope (Axio Observer Z1, Zeiss, Germany), covering an area of approximately 4200μm x 3200μm. Cell growth was analyzed by counting cells 6 h, 24 h, and 48 h after cell plating. Firstly, at 6 h the 20 nm condition was outpaced by the other conditions. At the 24 h timepoint the 20 nm condition and BI outpace the larger nanotubes in terms of cell proliferation. At the 48 h timepoint the BI is the clear forerunner, followed by the 20 nm condition, followed by the larger nanotubular conditions. These results agree with Park *et al*. and the Lai group's findings[57,67] in that the smaller nanotubular conditions produce more proliferation.

A novel finding is that the BI surface outperforms the smaller condition in terms of proliferation. This could be a result of the points of difference between the two conditions which include the hierarchical structure with a 40nm vertical height difference, along with differences in NND, wall thickness and Voronoi defects (slight disorder) and their interactions with protein adsorption and mechanotransduction with proteins, including vinculin. Furthermore, the average number of cells per condition actually saw a decrease from 6 h to 48 h in the 60 nm and 100 nm

conditions, which may indicate apoptosis as shown by previous literature by Park *et al*. which saw an increase in apoptotic rat MSCs in larger nanotube size ranges.[57] Interestingly the 20 nm condition saw a more rapid increase in growth overall compared to BI, however by 48 h the cellular proliferation with the 20 nm condition still had not caught up with the BI condition.

Cells are larger and more elongated in 20 nm and BI conditions

Whether or not an adherent cell can spread has vital consequences such as proliferation, quiescence or apoptosis.[45] Cell area and form factor were investigated through a custom Cellprofiler pipeline (Figures 22 and 23). To clarify, a form factor (calculated as $4*\pi*\text{Area}/\text{Perimeter}^2$) of 0 represents a linear cell and a form factor of 1 represents a circular cell. At 6 h the areas of the different conditions begin quite similarly, as the cells are beginning to initiate contact with the surface. At 24 h the 20 nm and BI conditions show distribution towards increase in area while in the 60 nm and 100 nm conditions cell areas remain similar to the 6 h timepoint. At 48 h the 20 nm and BI conditions clearly outdo the 60 nm and 100 nm conditions in terms of area. The 60 nm and 100 nm conditions show a decreased area at 48 h when compared to earlier timepoints. Regarding form factor, cells are similar at 6 h, neither elongated nor spherical across all conditions. At 24 h the 60 nm and 100 nm conditions show distribution towards increasing numbers of spherical cells while the 20 nm and BI present increased cellular elongation. At 48 h both the 60 nm and 100 nm conditions start to display distribution towards elongation while the BI condition shows the greatest elongation compared to all other conditions. As a qualitative check the numbers of elongated, multipolar and spherical cells were counted manually over all samples at 48 h and presented as a percentage (Figure 23). It was further confirmed that the 20 nm and BI conditions have a much greater number of elongated cells and conversely the spherical cells were much more widespread in the 60 nm and 100 nm conditions. Elongated cells

indicate cellular maturity and successful and sustained transduction of force from the surface through the integrin domains, to the FA proteins, actin cytoskeleton to the nucleus[68]. Similarly, Park *et al*. also found that cell spreading and adhesion of rat MSCs were severely impaired on nanotube conditions over 50nm.[57]

BI shows larger and more numerous Focal Adhesions

Focal adhesions (FAs) are important multimeric protein complexes which act as loci where integrin-mediated mechanosensation takes place, and is involved in vital cellular processes such as controlling cellular structure and shape, protein transport as well as organization of organelles. Focal adhesion analysis was performed on cells stained with Hoescht nuclear stain, actin (Rhodamine Red Phalloidin) and vinculin (AlexaFluor 488). Focal adhesion lengths and number/cell were characterized at 48 h (Figure 25, Tables 7 and 8). At 48 h the 20 nm and BI surfaces show many larger focal adhesions (>5 microns) and the 60 nm condition shows many medium-sized focal adhesions (2-4 microns), but lack larger adhesions. The 100 nm condition shows mainly smaller adhesions <2 microns in size, indicating a lack of mature adhesion capability on that surface. In terms of focal adhesion number, the BI surface shows a significantly larger number of focal adhesions/cell, followed by 20 nm condition, which is then followed by both the 60 nm and 100 nm conditions which have the least. This increase of focal adhesions may be due to the size of the cells, as larger cells found on the 20 nm and BI surface can accommodate and produce more and larger focal adhesions. Additionally the larger vertical surface area of the BI condition may contribute to increased protein adsorption, mechanotransduction and integrin binding. Similarly, Bauer *et al*. found that focal contact formation of rat MSCs was extensive on 15 nm nanotubes, but strongly reduced on uncoated 100 nm tube layers.[66]

20 nm and BI condition show Nuclear Elongation

As changes in cell morphology have been shown to influence nuclear shape which in turn may influence rates and specific gene transcription including cell proliferation and protein synthesis [46] the nuclear major axis length was measured over all conditions at 48 h (Figure 26). Results show that both the 20 nm and BI conditions had significantly elongated nuclei than the 60 nm and 100 nm conditions. This may be evidence towards differential patterns of gene transcription between the 20 nm and BI conditions and the 60 nm and 100 nm conditions.

All conditions show OSX localization to nucleus, Alizarin Red staining strongest on largest nanotubes

Biophysical elements of the stem cell environment are known to effect differentiation and therefore it is important to probe the details of our nanotubular surfaces in this regard. Osterix protein (OSX) was visualized using epifluorescence to probe extent of osteogenic differentiation via nuclear localization as an indicator of transcription. At 7 days (Figure 27) the OSX localized to the nucleus in every condition, indicating that the process of osteogenic differentiation had begun. At 28 days (Figures 28 and 29) the samples were stained with Alizarin red for visualization of calcium deposits. The lightest staining was observed on the control, with sparse to no redness, followed by the 20 nm condition, the 60 nm condition, BI, and finally the darkest red appeared on the 100 nm condition, with a thick layer almost appearing black in colour. This indicates that the condition which had the most calcium deposited was the 100 nm condition. Similarly, Wang *et al*.[69] performed a study which included OSX expression with nanotubular implants in minipigs and found that the expression increased in all nanotubular samples. In that study, OSX was increased the most on larger nanotube sizes (70nm and 100 nm), which may also corroborate with our Alizarin red results showing the lightest stain on the 20 nm nanotubes and darkest on the 100

nm nanotubes. The difference in the qualitative staining of Alizarin red between the 20 nm surface and BI may be attributed to the relative increase in nanoscale disorder present in the BI surface. It was shown by Dalby *et al*. that nanoscale disorder stimulates hMSCs to produce bone mineral *in vitro*.[12]

As a qualitative check on whether the cell filopodia were interacting with the nanotubular surfaces or not, SEM was carried out on fixed cells at 24 h (Figure 30). Indeed there were filopodial interactions on the nanoscale observed, as filopodia were seen to protrude over the nanotubes, which means that those mechanotransductive interactions between integrins, FA proteins and the actin cytoskeleton are reasonably posited.[33]

Conclusions and Future Outlook

In conclusion, chemical anodization was applied to a medically relevant metal in order to tune the surface nanotopography and in turn, four size conditions (20 nm, 60 nm, 100 nm) including a biomimetic substrate (which combines qualities of 20 nm and 100 nm in a hierarchical fashion) were created. In turn, spatial statistics such as nearest neighbor analysis and Voronoi analysis were successfully performed to quantitatively characterize the surfaces' order/disorder, topography and wettability analysis was also performed. All nanotubular surfaces were semiordered in nature, with the BI surface displaying relatively more disorder than the other conditions both on a local and global level. The nanotubes displayed increasing wettability as the size increased.

Moreover, human mesenchymal stem cell studies at short- and longer-term intervals were performed. The smaller nanotubes (20 nm) outperformed the larger nanotubes (60 nm, 100 nm) in terms of cell proliferation, cell area, elongation and focal adhesion size/number which indicates

more mature, polarizing cells with mature focal adhesions which transduce mechanical force continually from the surface to the actin cytoskeleton. These results agree with previous literature[57] on cell response to nanotubular surfaces. Surprisingly, the novel BI surface did as well as the 20 nm surface in the cellular studies and even outperformed the 20 nm nanotubes in terms of cell proliferation and focal adhesion number, which points to a need for future studies to examine the precise causes of such an effect and future uses for a hierarchical nanostructure. In terms of nuclei elongation the cells and their nuclei were significantly more elongated on the 20 nm and BI surfaces, a morphological change in the nucleus indicating genetic transcription of different proteins. Osteogenic differentiation analysis was also performed with OSX localization and Alizarin red studies. OSX was found to have localized to the nucleus in all sample conditions, and Alizarin Red staining revealed much darker staining on the large (100 nm) nanotubes than the other conditions, pointing towards possible increased mineralization in the larger nanotubes.

In surmising the reasons behind the improvement in BI over the 20 nm condition, Table 9 and Table 10 show the differences between the two conditions. BI 20 has the smallest wall thickness, with a 40nm difference between the 'lower' level and the 'higher level' as shown by AFM analysis, the closest NND between the smaller tubes on the lower level, and finally the distribution of the nanotubes is closer to disorder than order. This would be complement to literature which has shown that disorder produces higher adhesion and osteoblastic differentiation.[12] Additionally as previously stated the important portions of the FA including integrin tails, focal adhesion kinase (FAK), paxillin, talin and vinculin are all approximately 40nm away from the surface, which points to interesting future studies which may determine the 3D interactions between the BI surface walls and focal adhesion complexes, as the increased surface

area and precise 40nm vertical walls almost certainly entails additional cellular mechanotransductive effects.

This thesis investigated both the geometric characterization and cellular effects of 4 differential conditions of semiordered nanotubular topographies, and introduced a novel hierarchical surface for exploration of cellular behavior. The novel surface showed improved cellular effects, including proliferation and increased focal adhesions over the other surfaces and warrants further studies on the 3D nanotopography demonstrated therein. Moreover, a degree of spatial disorder as well as a vertical height were shown to have beneficial proliferative and spreading effects on cells. In addition to the novelty of a hierarchical nanosurface showing bioactive relevance, this is the first instance of a biomimetic surface structure (resembling a diatom frustule) being tested for its effects as a cellular biomaterial, which opens many doors for future studies in both cellular biomechanics and implant modification. Cells sense the complex ECM surface through focal adhesion proteins such as integrins binding to proteins on the surface, with focal adhesions being the anchor between cells and the ECM implicated in cell fate; therefore investigations into the protein adsorption on these nanosurfaces as a mediator between the surface and the cell are interesting future prospects. With further clarifications of the complex relationship between ECM proteins, nanotopography, focal adhesions and cell fate a novel third-generation biomaterial can be imagined. In the near future a simple tunable anodization process on ubiquitous titanium biomedical implants, in combination with small molecule drug encapsulation within the nanotubes may produce implants capable of directing cell fate while stimulating preferred cells to proliferate in the injured or diseased area.

Table 9. Summary of the geometric analysis. Highlighted are the unique characteristics of the BI surface.

Condition	Wall Thickness	Hierarchical Structure	Contact Angle	NND	Order (NND, Voronoi Area, Defects)
BI	Smallest(24nm)	Yes (40nm height)	Hydrophobic	Closest (44nm)	Tends towards disorder
20 nm	Large (55nm)	No	Hydrophobic	Close (65nm)	Tends towards order
60 nm	Medium (46nm)	No	Hydrophilic	Farther (88nm)	Tends towards order
100 nm	Small (32nm)	No	Hydrophilic	Farthest (109nm)	Tends towards order

Table 10. Summary of the cellular analysis. Highlighted are the unique cell response of the BI surface.

Condition	Proliferation	Cell Area	Form Factor/Morphology	Focal Adhesions	Nuclei	OSX localization to nucleus	Alizarin Red stain
BI	Highest	Large	Tends towards Elongated	Highest number	Elongated	Yes	Light
20 nm	High	Large	Tends towards Elongated	High number	Elongated	Yes	Lightest
60 nm	Low	Small	Tends towards Spherical	Low	Not elongated	Yes	High
100 nm	Low	Small	Tends towards Spherical	Low	Not elongated	Yes	Highest

References

1. Oldani, C., Dominguez, A. & Eli, T. Titanium as a Biomaterial for Implants.

2. Lee, K., Mazare, A. & Schmuki, P. One-Dimensional Titanium Dioxide Nanomaterials : Nanotubes. (2014).

3. Kulkarni, M. *et al.* Titanium nanostructures for biomedical applications. **26,** (2015).

4. Mahdavi, A. *et al.* A biodegradable and biocompatible gecko-inspired tissue adhesive. **105,** 1–6 (2008).

5. Wegst, U. G. K., Bai, H., Saiz, E., Tomsia, A. P. & Ritchie, R. O. Bioinspired structural materials. **14,** 23–36 (2015).

6. Garcia, A. P., Sen, D. & Buehler, M. J. Hierarchical Silica Nanostructures Inspired by Diatom Algae Yield Superior Deformability , Toughness , and Strength. **42,** (2011).

7. Cai, J., Pan, J., Chen, M., Wang, Y. & Zhang, D. Culturing and Bonding of Diatom on a Microfluidic Chip for Biosensing Application. **461,** 809–813 (2014).

8. Chandrasekaran, S. *et al.* Silicon diatom frustules as nanostructured photoelectrodes. *Chem. Commun.* **50,** 10441–10444 (2014).

9. Roy, P., Berger, S. & Schmuki, P. TiO 2 Nanotubes : Synthesis and Applications Angewandte. 2904–2939 (2011). doi:10.1002/anie.201001374

10. Sjöström, T. *et al.* Titanium nanofeaturing for enhanced bioactivity of implanted orthopedic and dental devices. *Nanomedicine (Lond).* (2013). doi:10.2217/nnm.12.177

11. Dalby, M. J., Gadegaard, N. & Oreffo, R. O. C. Harnessing nanotopography and integrin-matrix interactions to influence stem cell fate. *Nat. Mater.* **13,** 558–569 (2014).

12. Dalby, M. J. *et al.* The control of human mesenchymal cell differentiation using nanoscale symmetry and disorder. (2007). doi:10.1038/nmat2013

13. Lee, J.-K., Choi, D.-S., Jang, I. & Choi, W.-Y. Improved osseointegration of dental titanium implants by TiO2 nanotube arrays with recombinant human bone morphogenetic protein-2: a pilot in vivo study. *Int. J. Nanomedicine* (2015). doi:10.2147/IJN.S78138

14. Bessegato, G. G., Guaraldo, T. T. & Zanoni, M. V. B. in (ed. Aliofkhazraei Surface and Corrosion Science, M. B. T.-M. E. M. in N.) Ch. 10 (InTech, 2014). doi:10.5772/58333

15. Robin, A. *et al.* Formation of TiO 2 nanotubes produced by anodization in ethylene glycol-H2O electrolyte Experimental procedure. *J. Surf. Eng. Mater. Adv. Technol.* (2014).

16. Anodic TiO 2 nanotube layers: why does self-organized growth occur - A mini review Xuemei Zhou.

17. Raja, K. S., Gandhi, T. & Misra, M. Effect of water content of ethylene glycol as electrolyte for synthesis of ordered titania nanotubes. *Electrochem. commun.* **9,** 1069–1076 (2007).

18. Wang, B. D., Yu, B., Wang, C., Zhou, F. & Liu, W. A Novel Protocol Toward Perfect Alignment of Anodized TiO 2 Nanotubes. **100039,** 1964–1967 (2009).

19. Moreno, M. D., Ma, K., Schoenung, J. & Dávila, L. P. An integrated approach for probing the structure and mechanical properties of diatoms: Toward engineered nanotemplates. *Acta Biomater.* **25,** 313–324 (2015).

20. Gordon, R., Sterrenburg, F. A. S. & Sandhage, K. H. A Special Issue on Diatom

Nanotechnology. *J. Nanosci. Nanotechnol.* (2005). doi:10.1166/jnn.2005.017

21. Jang, D., Meza, L. R., Greer, F. & Greer, J. R. Fabrication and deformation of three-dimensional hollow ceramic nanostructures. **12,** (2013).

22. Bansal, P. P. & Ardell, A. J. Average nearest-neighbor distances between uniformly distributed finite particles. *Metallography* (1972). doi:10.1016/0026-0800(72)90048-1

23. Mitchel A., E. The ESRI Guide to GIS analysis, Volume 2: Spartial measurements and statistics. *ESRI Guide to GIS analysis* (2005).

24. Reem, D. The geometric stability of Voronoi diagrams with respect to small changes of the sites. 1–30 (2011). doi:10.1145/1998196.1998234

25. Ratto, F., Johnston, T. W., Heun, S. & Rosei, F. A numerical approach to quantify self-ordering among self-organized nanostructures. *Surf. Sci.* **602,** 249–258 (2008).

26. Lindner, U. & Schlenke, P. Mesenchymal Stem or Stromal Cells : Toward a Better Understanding of Their Biology ? 75–83 (2010). doi:10.1159/000290897

27. Lutolf, M. P., Gilbert, P. M. & Blau, H. M. Designing materials to direct stem-cell fate. **462,** (2009).

28. Kim, J. *et al.* Designing nanotopographical density of extracellular matrix for controlled. 1–11 (2013). doi:10.1038/srep03552

29. Liu, J. *et al.* Talin determines the nanoscale architecture of focal adhesions. *Proc. Natl. Acad. Sci.* **112,** E4864–E4873 (2015).

30. Dalby, M. J., Gadegaard, N. & Oreffo, R. O. C. Harnessing nanotopography and integrin–

matrix interactions to influence stem cell fate. *Nat. Publ. Gr.* **13,** 558–569 (2014).

31. Winograd-katz, S. E. & Geiger, B. The integrin adhesome : from genes and proteins to human disease. doi:10.1038/nrm3769

32. Wolfenson, H., Lavelin, I. & Geiger, B. Review Dynamic Regulation of the Structure and Functions of Integrin Adhesions. *Dev. Cell* **24,** 447–458 (2013).

33. Swaminathan, V. & Waterman, C. M. The molecular clutch model for mechanotransduction evolves. *Nat. Publ. Gr.* **18,** 459–461 (2016).

34. Wolfenson, H., Lavelin, I. & Geiger, B. Review Dynamic Regulation of the Structure and Functions of Integrin Adhesions. *Dev. Cell* **24,** 447–458 (2013).

35. Kass, L., Janine T. Erler, M. D. & Weaver, and V. M. Mammary epithelial cell: Influence of extracellular matrix composition and organization during development and tumorigenesis. *Int. J. Biochem. Cell Biol.* (2007).

36. Jiang, G., Huang, A. H., Cai, Y., Tanase, M. & Sheetz, M. P. Rigidity sensing at the leading edge through alphavbeta3 integrins and RPTPalpha. *Biophys. J.* (2006). doi:10.1529/biophysj.105.072462

37. Swaminathan, V. & Waterman, C. M. The molecular clutch model for mechanotransduction evolves. *Nat. Publ. Gr.* **18,** 459–461 (2016).

38. Humphries, J. D. *et al.* Vinculin controls focal adhesion formation by direct interactions with talin and actin. *J. Cell Biol.* **179,** 1043–1057 (2007).

39. Montanez, E. *et al.* Kindlin-2 controls bidirectional signaling of integrins. *Genes Dev.* (2008). doi:10.1101/gad.469408

40. Yu, C. -h., Law, J. B. K., Suryana, M., Low, H. Y. & Sheetz, M. P. Early integrin binding to Arg-Gly-Asp peptide activates actin polymerization and contractile movement that stimulates outward translocation. *Proc. Natl. Acad. Sci.* (2011). doi:10.1073/pnas.1109485108

41. Choi, C. K. *et al.* Actin and α-actinin orchestrate the assembly and maturation of nascent adhesions in a myosin II motor-independent manner. *Nat. Cell Biol.* (2008). doi:10.1038/ncb1763

42. Vicente-Manzanares, M. & Horwitz, A. R. Cell migration: An overview. *Methods in Molecular Biology* (2011). doi:10.1007/978-1-61779-207-6_1

43. Gardel, M. L., Schneider, I. C., Aratyn-Schaus, Y. & Waterman, C. M. Mechanical Integration of Actin and Adhesion Dynamics in Cell Migration. *Annu. Rev. Cell Dev. Biol.* **26,** 315–333 (2010).

44. Gauthier, N. C., Masters, T. A. & Sheetz, M. P. Mechanical feedback between membrane tension and dynamics. *Trends Cell Biol.* **22,** 527–535 (2012).

45. McGrath, J. L. Cell Spreading: The Power to Simplify. *Curr. Biol.* **17,** 357–358 (2007).

46. Chen, B., Co, C. & Ho, C.-C. Cell Shape Dependent Regulation of Nuclear Morphology Bo. *Biomaterials* **67,** 129–136 (2015).

47. Tapley, E. C. & Starr, D. A. Connecting the nucleus to the cytoskeleton by SUN-KASH bridges across the nuclear envelope. *Curr. Opin. Cell Biol.* **25,** 57–62 (2014).

48. Bridger, J. M., Boyle, S., Kill, I. R. & Bickmore, W. A. Re-modelling of nuclear architecture in quiescent and senescent human fibroblasts. *Curr. Biol.* (2000).

doi:10.1016/S0960-9822(00)00312-2

49. Amorim, B. R. *et al.* The transcriptional factor Osterix directly interacts with RNA helicase A. *Biochem. Biophys. Res. Commun.* **355,** 347–351 (2007).

50. Tai, G., Christodoulou, I., Bishop, A. E. & Polak, J. M. Use of green fluorescent fusion protein to track activation of the transcription factor osterix during early osteoblast differentiation. *Biochem. Biophys. Res. Commun.* (2005). doi:10.1016/j.bbrc.2005.05.195

51. Gregory, C. A., Gunn, W. G., Peister, A. & Prockop, D. J. An Alizarin red-based assay of mineralization by adherent cells in culture: Comparison with cetylpyridinium chloride extraction. *Anal. Biochem.* **329,** 77–84 (2004).

52. Uccelli, A., Moretta, L. & Pistoia, V. Mesenchymal stem cells in health and disease. *Nat. Rev. Immunol.* **8,** 726–736 (2008).

53. Park, J. *et al.* TiO 2 Nanotube Surfaces : 15 nm — An Optimal Length Scale of Surface Topography for Cell Adhesion and Differentiation **. 666–671 (2009). doi:10.1002/smll.200801476

54. Park, J., Bauer, S., Von Der Mark, K. & Schmuki, P. Nanosize and vitality: TiO2 nanotube diameter directs cell fate. *Nano Lett.* **7,** 1686–1691 (2007).

55. Oh, S. *et al.* Stem cell fate dictated solely by altered nanotube dimension. (2009).

56. von der Mark, K., Bauer, S., Park, J. & Schmuki, P. Another look at 'Stem cell fate dictated solely by altered nanotube dimension'. *Proc. Natl. Acad. Sci.* **106,** E60–E60 (2009).

57. Park, J. *et al.* TiO2 nanotube surfaces: 15 nm - an optimal length scale of surface

topography for cell adhesion and differentiation. *Small* **5,** 666–671 (2009).

58. Yu, W. Q., Jiang, X. Q., Zhang, F. Q. & Xu, L. The effect of anatase TiO2 nanotube layers on MC3T3-E1 preosteoblast adhesion, proliferation, and differentiation. *J. Biomed. Mater. Res. - Part A* (2010). doi:10.1002/jbm.a.32687

59. Paulose, M. *et al.* Anodic growth of highly ordered TiO2 nanotube arrays to 134 microm in length. *J. Phys. Chem. B* (2006). doi:10.1021/jp064020k

60. Zhukova, Y. *et al.* The Role of Titanium Surface Nanostructuring on Preosteoblast Morphology, Adhesion, and Migration. *Adv. Healthc. Mater.* **6,** 1–13 (2017).

61. Buxboim, A., Ivanovska, I. L. & Discher, D. E. Matrix elasticity, cytoskeletal forces and physics of the nucleus: how deeply do cells 'feel' outside and in? *J. Cell Sci.* (2010). doi:10.1242/jcs.041186

62. Yang, W. *et al.* Titania nanotubes dimensions-dependent protein adsorption and its effect on the growth of osteoblasts. *J. Biomed. Mater. Res. - Part A* **102,** 3598–3608 (2014).

63. Coyer, S. R. *et al.* Nanopatterning reveals an ECM area threshold for focal adhesion assembly and force transmission that is regulated by integrin activation and cytoskeleton tension. *J. Cell Sci.* (2012). doi:10.1242/jcs.108035

64. Kanchanawong, P. *et al.* Nanoscale architecture of integrin-based cell adhesions. *Nature* (2010). doi:10.1038/nature09621

65. Carisey, A. *et al.* Vinculin regulates the recruitment and release of core focal adhesion proteins in a force-dependent manner. *Current Biology* (2013). doi:10.1016/j.cub.2013.01.009

66. Bauer, S., Park, J., Mark, K. von der & Schmuki, P. Improved attachment of mesenchymal stem cells on super-hydrophobic TiO2 nanotubes. *Acta Biomater.* (2008). doi:10.1016/j.actbio.2008.04.004

67. Lai, M. *et al.* Surface functionalization of TiO2 nanotubes with bone morphogenetic protein 2 and its synergistic effect on the differentiation of mesenchymal stem cells. *Biomacromolecules* **12,** 1097–1105 (2011).

68. Bays, J. L. *et al.* Vinculin phosphorylation differentially regulates mechanotransduction at cell-cell and cell-matrix adhesions. *J. Cell Biol.* **205,** 251–263 (2014).

69. Wang, N. *et al.* Effects of TiO2nanotubes with different diameters on gene expression and osseointegration of implants in minipigs. *Biomaterials* **32,** 6900–6911 (2011).